The Precipitation and Radiative Responses to Convective Organization in the Tropical North Atlantic

Juliet A. Pilewskie

A thesis submitted in partial fulfillment of

the requirements for the degree of

Master of Science

(Atmospheric and Oceanic Sciences)

at the

University of Wisconsin-Madison

2019

Abstract

The Precipitation and Radiative Responses to Convective Organization in the Tropical North Atlantic

by Juliet A. Pilewskie

Improved representation of the processes involved in organizing convection and the associated high cloud feedbacks is a key challenge facing weather and climate models. One form of convective organization that occurs in idealized numerical model simulations is self-aggregation, or randomly distributed convection becoming localized despite homogeneous boundary conditions. Convective aggregation has the potential to influence climate by reducing the area of detrained high cloud cover and drying the mean state of the atmosphere, which impact both precipitation production and radiative effects. In order to assess the underlying processes influencing convective organization, four years of CloudSat and A-train cloud, precipitation, and radiation datasets are analyzed in the context of collocated time-evolving geostationary cloud property datasets from the PATMOS-x climate record. It is found that convective intensity and precipitation yield only weakly depend on large-scale circulation. Storm area increases with convective intensity in strong subsidence environments more than in environments with strong ascent. In both dynamical environments, the cooling effect of convective clouds decreases with increasing intensity, implying that a shift toward more intense convection may transition the high cloud feedback from a cooling effect to a neutral or possibly warming effect on Earth's climate.

Acknowledgements

I would first like to thank my advisor, Tristan L'Ecuyer, without whom none of this work would have been possible. Under his guidance, I have learned to ask and obtain answers to insightful, yet straightforward questions, and to be creative when refining analyses. Tristan has expanded my passion for this field—with every meeting I end up having more questions afterwards than I have at the beginning, but my enthusiasm for obtaining answers usually increases tenfold. I am very grateful to have a dedicated and hard-working mentor to propel my graduate studies.

I would also like to thank the two other readers of my thesis, Larissa Back and Stephanie Henderson who both provided me with great insight on how to better not just the thesis but myself as a scientist.

I would also like to thank former members of the L'Ecuyer group: Kate Sauter and Tobiah Steckel who provided me with some of the code and data sets that got me started on this project. Tobiah was always very willing to assist me in explaining and debugging code. Ethan Nelson and Elin McIlhattan were also willing and helpful in answering my questions about my methods despite no longer living in Wisconsin. Many thanks to the rest of the L'Ecuyer group: Norm Wood, Aronne Merrelli, Claire Pettersen, David Henderson, Marian Mateling, Alyson Douglas, April Hang, Andrew Dzambo, Julia Shates, Anne Sledd, Ashtin Massie, and James Anheuser for all of their support and constructive criticism when supplying feedback on presentations and/or proposal and thesis drafts.

Many thanks to Pete Pokrandt for his tireless work on helping me with all of the computer issues that I ran into. Also thanks to the AOS administrative group: Sue Foldy, Chelsea Dahman, Dee Van Ruyven, and Sonja Johnson, and all of the rest of the AOS faculty.

Last but not least, I would like to thank my family, Peter, Kathy, and Monica, for their never-ending love and support in everything that I do. I do not know where I would be without them. Many many thanks to my wonderful friends in Madison, both in AOS and outside of it. They have introduced me to this beautiful town and made me feel very welcome, and I am forever grateful.

Acknowledgement is made to the CloudSat Data Processing Center for CloudSat Data and to the CIMSS Climate Data Portal for PATMOS-x data.

This work was supported by the CloudSat/CALIPSO team.

Contents

List of Figures

Abbreviations

ABI	**A**dvanced **B**aseline **I**mager
ACHA	**A**BI **C**loud **H**eight **A**lgorithm
AIRS	**A**tmospheric **I**nfra**r**ed **S**ounder
AMSR-E	**A**dvanced **M**icrowave **S**canning **R**adiometer - **E**arth Observing System
AMSU-A	**A**dvanced **M**icrowave **S**ounding **U**nit-A
A-Train	**A**fternoon **Train**
AVHRR	**A**dvanced **V**ery **H**igh **R**esolution **R**adiometer
CALIOP	**C**loud-**A**erosol **L**idar with **Orthogonal P**olarization
CALIPSO	**C**loud-**A**erosol **L**idar and **I**nfrared **P**athfinder **S**atellite **O**bservation
CAPE	**C**onvective **A**vailable **P**otential **E**nergy
CERES	**C**louds and the **E**arth's **R**adiant **E**nergy **S**ystem
COG	**C**enter **O**f **G**ravity
CPR	**C**loud **P**rofiling **R**adar (aboard CloudSat)
CRE	**C**loud **R**adiative **E**ffect

CRF	**C**loud **R**adiative **F**orcing
CRM	**C**loud **R**esolving **M**odel
CTT	**C**loud **T**op **T**emperature
CWV	**C**olumn **W**ater **V**apor
DCOMP	**D**aytime **C**loud **O**ptical and **M**icrophysical **P**roperties
DJF	**D**ecember, **J**anuary, **F**ebruary
GCM	**G**eneral **C**irculation **M**odel
GEOPROF	**Geo**metric **Prof**ile
GEOS-5 DAS	**G**oddard **E**arth **O**bserving **S**ystem **D**ata **A**nalysis **S**ystem, Version 5
GOES	**G**eostationary **O**perational **E**nvironmental **S**atellite system
ECMWF	**E**uropean **C**entre for **M**edium-Range **W**eather **F**orecasts
EOS	**E**arth **O**bserving **S**ystem
EUMETSAT	**Eu**ropean Organisation for the Exploitation of **Met**eorological **Sat**ellites
IPCC AR5	**I**ntergovernmental **P**anel on **C**limate **C**hange Fifth **A**ssessment **R**eport
IIR	**I**maging **I**nfrared **R**adiometer
IR	**I**nfra**r**ed
ITCZ	**I**nter **T**ropical **C**onvergence **Z**one
JJA	**J**une, **J**uly, **A**ugust
LW	**L**ong**w**ave

MAM	**M**arch, **A**pril, **M**ay
MERRA	**M**odern-**E**ra **R**etrospective analysis for **R**esearch and **A**pplications
MetOp	**M**eterological **O**peration
MJO	**M**adden-**J**ulian Oscillation
MODIS	**Mod**erate Resolution **I**maging **S**pectroradiometer
MSG	**M**eteosat **S**econd **G**eneration
NOAA	**N**ational **O**ceanic and **A**tmospheric **A**dministration
PAROSOL	**P**olarization & **A**nisotropy of **R**eflectances for **A**tmospheric **S**ciences coupled with **O**bservations from a **L**idar
PATMOS-x	**P**athfinder **Atmos**pheres - E**x**tended
OLR	**O**utgoing **L**ongwave **R**adiation
RCE	**R**adiative-**C**onvective **E**quilibrium
SCAI	**S**imple **C**onvective **A**ggregation **I**ndex
SON	**S**eptember, **O**ctober, **N**ovember
SST	**S**ea **S**urface **T**emperature
SW	**S**hort**w**ave
TOA	**T**op-**o**f-**A**tmosphere
WFC	**W**ide **F**ield **C**amera

Chapter 1

Introduction

1.1 What is Convection?

When you turn a kettle on to boil, you notice that the water in the kettle warms uniformly. This process, known as convection, transfers energy from warmer regions to cooler regions. The warm regions are less dense than the cool regions, so warm water rises and cool water sinks—allowing for the water to mix. Convection can occur not just in liquid water, but in all fluids; thus, almost all of the vertical motions in the Earth's atmosphere and ocean result from convection. The prominent driver of convection in the atmosphere and ocean is incoming solar radiation that heats the Earth's surface. As warm air rises from the surface and through the atmosphere, it cools, expands, and the water vapor that it contains condenses. The phase change releases energy to the surroundings that warms the atmosphere. Without this additional warming, the atmosphere would cool at a much quicker rate. Thus, a balance forms between radiative cooling by radiation that Earth's surface emits and convective warming by energy released to the surroundings

from water vapor condensing into cloud droplets and precipitation.

Deep atmospheric convection spans over 10 km vertically and is largely concentrated in summer monsoon regions, along the Inter Tropical Convergence Zone (ITCZ), along the slopes and crests of mountain ranges, and within the frontal zones and warm sectors of extratropical cyclones. Clouds and thunderstorms that result are often organized into clusters that contain many individual cells. They vary both on spatial and temporal scales, spanning from squall lines that last for at most an hour to large-scale convective activity prevalent in Madden-Julian Oscillation (MJO) events that can persist for a week. Convective systems contribute to momentum and moisture budgets, transport energy meridionally, and alter the Earth's energy budget.

While convective systems cover only a few percent of the surface area of the tropics and subtropics, they strongly influence large-scale circulation (Riehl and Malkus, 1958, Riehl and Simpson, 1979) through their contributions to the tropics' water cycle and radiative energy budget. Convective systems make up the majority of the rainfall in the tropics (Houze, 2004, Nesbitt et al., 2000). Large-scale rising motion, convection, and precipitation are predominantly found along the narrow ITCZ band, which is also known as the ascending branch of the Hadley cell. Individual meridional circulation cells that are driven by energy from direct solar insolation comprise the ascending motion. These convective cells are fueled by air that converges at the surface, also known as trade winds. As illustrated in Figure 1.1, cumuliform clouds, ranging from shallow to deep and expansive clouds, form in the narrow ITCZ band. The descending branch of the Hadley

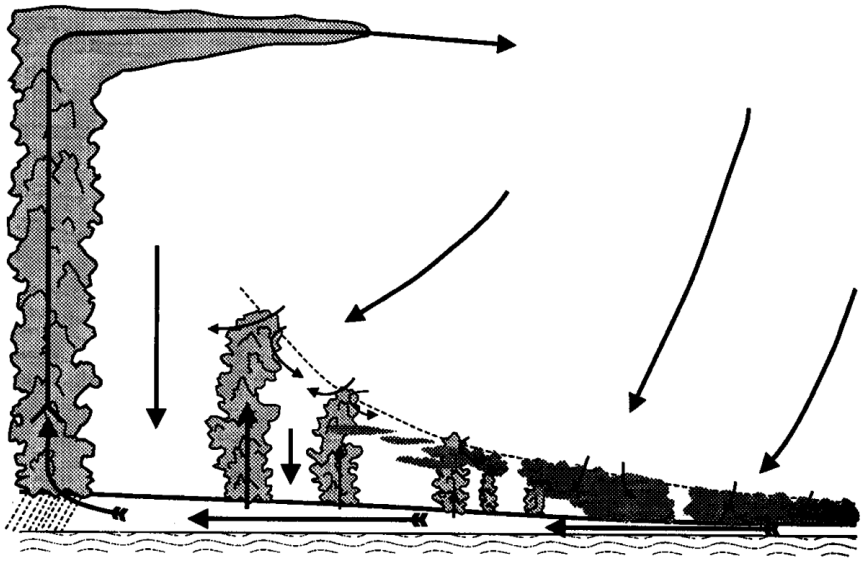

FIGURE 1.1: Structure of the tropical atmosphere in regions varying in large-scale vertical motion. Illustration courtesy of (Emanuel, 1994).

cell is located in the subtropics and consists of dry and clear regions as well as low-level boundary, or stratus, clouds formed from large-scale atmospheric subsidence. The ascending and descending branches of the Hadley cell balance each other through radiative cooling in the subsidence regions and latent heating from water vapor condensation in the ascending regions' precipitating clouds.

1.2 Radiative and Thermodynamic Impacts of Convection

Clouds influence the radiative balance (Liou, 1986) at the top-of-atmosphere (TOA) through their properties of reflecting, absorbing, and transmitting radiation to the Earth's surface and out of the atmosphere. Their impact on both solar and terrestrial radiation depend on the cloud particles and cloud morphology. Cloud top temperature

(CTT) at TOA can be used as a measure of how much net upward longwave (LW) radiative flux reduces due to clouds. This reduction in outgoing LW radiation (OLR), or the LW cloud radiative effect (LW CRE), is strongest for high, cold clouds with low CTTs and introduces a warming effect on Earth's surface. LW CRE is a positive quantity, while shortwave (SW) CRE is a negative quantity at TOA because it is a measure of how much incoming solar radiation is being reflected out of the atmosphere. SW CRE depends on the liquid and ice water path, as well as cloud particle size and habit, and has a cooling effect on Earth's surface. The total CRE at TOA is known as the net CRE.

The left panel in Figure 1.2 shows the net CRE as a function of CTT and optical depth. Shallow clouds, or clouds that lie low in the atmosphere such as stratus largely found in the subtropics, contribute to the lower right corner of the plot because they have high optical depths to reflect incoming solar radiation and warm CTTs that make them inefficient at reducing OLR from Earth's surface. In a climate context, shallow clouds have a net cooling effect. The right panel in Figure 1.2 portrays the fractional coverage of clouds in East Pacific as a function of MODIS-derived CTTs and visible optical depths. From this figure, it is apparent that deep convective clouds have strong LW and SW influences so that their net radiative impact is near-zero.

Both thermodynamic and radiative processes associated with convective cloud clusters' formation and evolution are sufficiently strong enough to alter the vertical profiles of heating (Houze Jr., 1982). These processes significantly influence large-scale vertical motion in the tropics (Houze Jr., 1982), and have varying impacts over convective systems' lifecycle. The lifecycle of a single convective cell can be broken up into three stages:

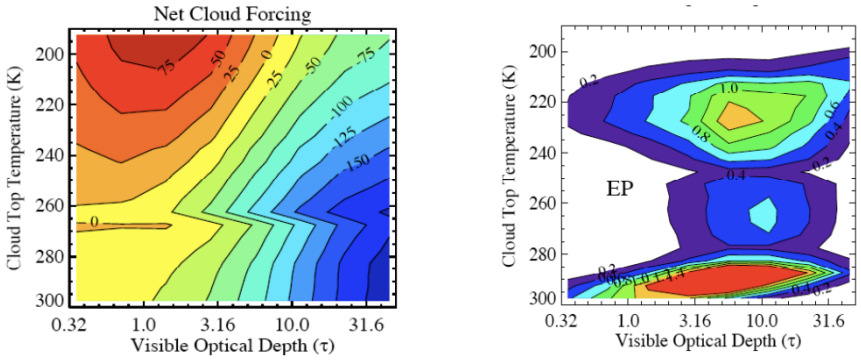

FIGURE 1.2: (a) Net effect of tropical clouds on the radiation budget at the top-of-atmosphere as a function of cloud top temperature and cloud optical depth. (b) MODIS-derived histogram of East Pacific ITCZ cloud cover (units are percent cloud fraction per bin) binned by visible optical depths and cloud-top temperature. Image courtesy of Kubar et al. (2007).

cumulus, *mature*, *dissipating*. Both radiation and surface fluxes from heat and water vapor destabilize the atmosphere, which initiates moist convection that acts as a stabilizing mechanism. The cumulus stage is defined by a warm buoyant plume rising, mixing laterally with the environment, and forming a cloud that is optically thick and reflects some incoming SW radiation but is relatively small across spatial scales. This allows for OLR from the surface to escape to space.

As it begins to rain, a downward drag force induced by rain drops instigates a vigorous downdraft circulation that is evident in the mature stage. The downdraft region is also responsible for the heaviest rainfall within the system, which supplies the latent heating sufficient for the system to continue to be invigorated. The maximum updraft vertical velocities are in the middle of the cloud, with detrainment occurring above this level. As the top of the cloud approaches the tropopause, clouds spread around the overshooting top into what is known as cirriform anvil. At this stage there is significant cloud cover in both the horizontal and vertical direction for the radiative impacts of this

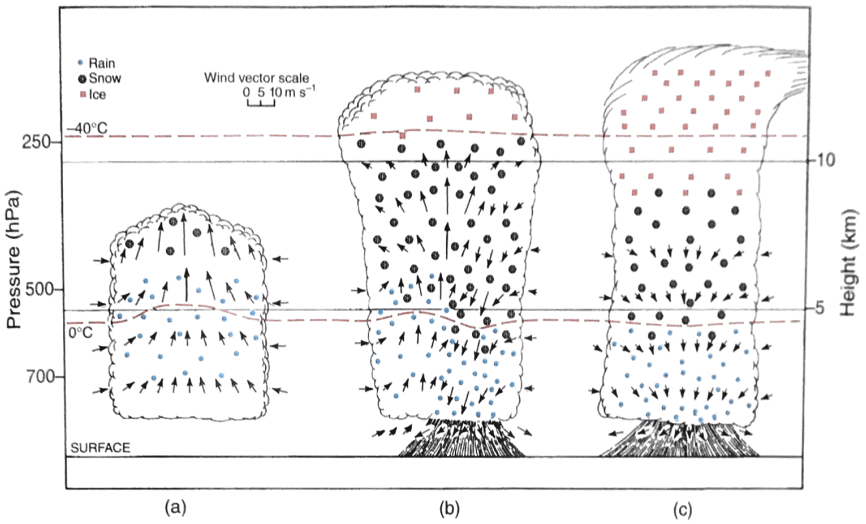

FIGURE 1.3: Three-stage lifecycle of a typical convective cell showing (a) cumulus stage, (b) mature stage, and (c) dissipating stage. Illustration courtesy of Wallace and Hobbs (2006) adapted from *The Thunderstorm*, U.S. Government Printing Office (1949).

system to be significant. The large spread in anvil weakens radiative cooling because of the low brightness temperatures emitted from the high anvils compared to OLR from Earth's surface or from shallow clouds. Anvils that are sufficiently thick can have a large impact on reflecting SW radiation to space (Ramanathan and Collins, 1991). During the dissipating stage, cloud droplets no longer grow, so precipitation stops. Vertical air motions also weaken and die, while the upper level clouds remain for a while emitting and absorbing radiation. Upper clouds thin out and break up, which reduces the SW cloud forcing and enhances LW forcing (Houze Jr., 1982).

1.3 Quantifying High Cloud Feedbacks

1.3.1 Uncertainties in Climate Models

Throughout their lifecycle, convective systems alter the spatiotemporal patterns of radiative heating and cooling at TOA, which impact the large-scale atmospheric circulation (Randall et al., 1989, Slingo and Slingo, 1988, 1991). As the climate changes, changes in large-scale circulation are expected to alter convective cloud formation and their radiative responses—generating a feedback (Bony et al., 2015, Li et al., 2014, Sherwood et al., 2014). Climate models make predictions of climate warming by measuring the "climate sensitivity", which is the equilibrium change in the globally averaged near-surface temperature in response to a doubling of the concentration of atmospheric CO_2. According to the Intergovernmental Panel on Climate Change (IPCC) Fifth Assessment Report (AR5), the climate sensitivity is in the range of 1.5 to 4.5 K with a weak increase in global mean precipitation (IPCC, 2013, Stephens and Ellis, 2008). Climate warming is expected to influence the distribution of precipitation changes, with the wettest latitudes getting enhanced precipitation while driest latitudes may get a decrease in precipitation (Allen and Ingram, 2002, Held and Soden, 2006, Mitchell, 1987). Additionally, atmospheric general circulation models (GCMs) are showing that precipitation extremes become more frequent with enhanced atmospheric CO_2 concentrations (Gordon et al., 1992).

Observations suggest that the climate sensitivity is near the lower end of the 3 K temperature range and that models could also be underestimating precipitation changes

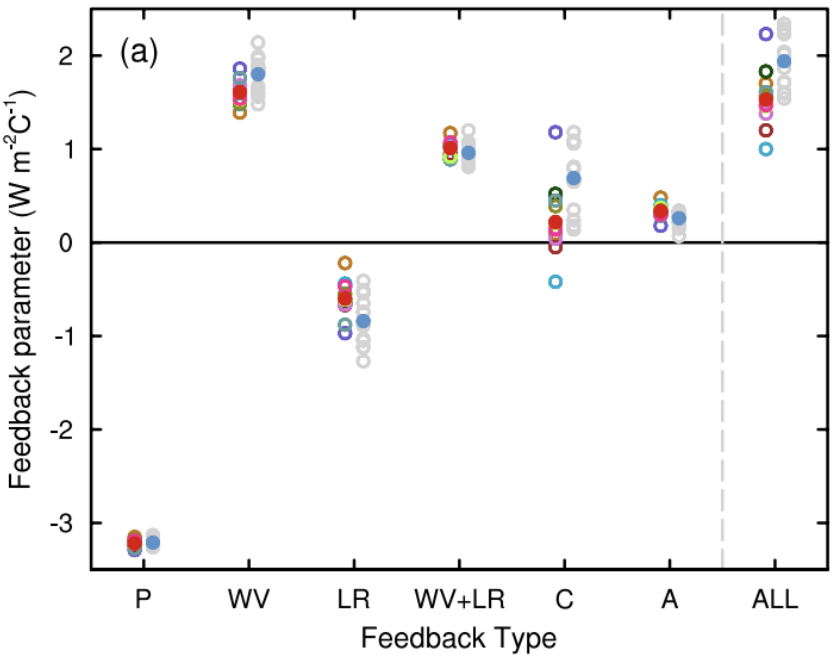

FIGURE 1.4: Strengths of individual feedbacks from CMIP3 (right column of gray circles) and CMIP5 (left column of colored circles) models for different feedback types (C: Cloud). The filled red circles correspond to CMIP5 means and filled blue circles are the CMIP3 means for each feedback type. Illustration courtesy of IPCC AR5.

(Mauritsen and Stevens, 2015). These discrepancies point to the possibility that climate models are missing key feedbacks or that the processes that drive cloud-circulation interactions are poorly represented (Dessler, 2013, Mauritsen and Stevens, 2015). In addition to the discrepancies between models and observations, there are disagreements between the models themselves. The 3 K climate sensitivity range is largely due to a substantial spread in cloud feedbacks among climate models, as shown in Figure 1.4. A major source of uncertainty contributing to the large spread is how convective and boundary-layer processes are represented in climate models (Bony et al., 2015). Additionally, cloud microphysical processes make it difficult to simulate convective response to varying large-scale dynamics.

Observations have been used to supply information for models on the thermodynamic processes, dynamical influences, and cloud microphysics of convective organization. Satellite infrared (IR) images provide reliable cloud coverage with high temporal and spatial resolution (e.g. Gettelman et al. (2002), Hall and Vonder Haar (1999), Mapes and Houze (1993), Rossow and Schiffer (1999)) capable of characterizing the regional and global characteristics of convection. Studies using radar and passive microwave observations provide direct information on the vertical intensity of such systems (e.g. Liu and Zipser (2005), Mohr and Zipser (1996), Nesbitt et al. (2006, 2000), Schumacher and Houze (2003)). Liu et al. (2007) and Liu and Zipser (2013) provided two of the first studies to quantitatively explore the relationship between high, cold anvil clouds and the vertically intense convection using observations on a global scale. Such analyses optimize the advantages of passive and active satellite observations by looking at them together (Liu et al., 2007).

1.3.2 Theories on High Cloud Feedbacks

The radiative impacts of convective systems depends both on the dynamic and thermodynamic structures of the atmosphere (Bony et al., 2004, Lindzen et al., 2001, Pierrehumbert, 1995, Ramanathan and Collins, 1991). With a warming climate, it is expected that the temperature profile, atmospheric moisture, and large scale circulation will change—all of which impact the formation and distribution of clouds (Bony et al., 2004, Bony et al., 1997, Hartmann and Michelsen, 1993). There is observational evidence for a shift toward more frequent organized convection with warming in the past 30 years

(Tselioudis et al., 2010), which has resulted in an increase tropical rainfall intensity (Tan et al., 2015) and has the potential to alter the formation of high anvil clouds (Bony et al., 2016).

Arguments for assessing the behavior of anvil clouds to a warming climate and the suggested climate feedbacks have been proposed over the past several years. Ramanathan and Collins (1991) used observations during the 1987 El Niño to argue that Hadley and Walker Cells fueled by latent heating, cirrus LW CRE, and spatial gradients in sea surface temperature (SST) causes moisture to converge into the warm oceanic regions. This amplifies SST warming through enhanced atmospheric greenhouse effect, which impacts atmospheric circulation. Ramanathan and Collins (1991) proposed the "Thermostat Hypothesis" that argued that enhanced SST warming could increase cirrus cloud formation to reflect enough solar radiation to offset LW CRE and prevent SST from rising above 305 K (Ramanathan and Collins, 1991).

Lindzen et al. (2001) proposed that the Earth's atmosphere can act as an adaptive infrared iris, much like that of an eye, which opens and closes in order to control OLR. This was supported by suggesting that cirrus detrainment from cumulus convection might decrease with increasing SSTs if the precipitation efficiency within cumulus towers increases significantly with increasing SSTs (Lindzen et al., 2001). The Iris Effect would cause the sensitivity of surface temperature to a doubling of CO_2 to be only 1 K, which is significantly less than the largely accepted range of 1.5-4.5 K.

The Thermostat and Infrared Iris Hypotheses have opposing arguments—Thermostat argues that anvil fraction will increase and Infrared Iris argues that anvil fraction will

decrease with increasing SST—that both result in a cooling effect on Earth's climate. The Iris effect doesn't take into account how anvil cloud brightness impacts SW radiation, so the effect would weaken if thick anvil clouds are reduced more strongly than thin anvils because SW reflectivity by these systems would decrease. Because high clouds exert both warming and cooling effects, it is the net effect of high cloud changes that is important and is also responsible for the discrepancy between these theories. The high cloud net radiative effect arises from the difference between the SW and LW—two large, competing effects—which makes high cloud effects on the Earth's radiative energy budget very hard to quantify both in models and observations. Understanding how thick and thin anvils form, as well as how they may change with climate change, will improve quantifying high cloud feedbacks.

1.4 Convective Aggregation

Model studies are beneficial for postulating ways in which the environment influences convection and the corresponding radiative and precipitation effects contributing to a climate response. One of the arguments against the Infrared Iris hypothesis was that there was a significant amount of space, on the order of 1000 km, in between the deep convective cores and the decreasing anvils (Hartmann and Michelsen, 2002). However, theories suggest that these large patches of clear, dry air could be tied to increased subsidence as a result of convective aggregation, which is a phenomena arising from instabilities in idealized models. This implies that convective aggregation could be a physical mechanism in support of an Infrared Iris-like response to increasing SSTs (Mauritsen and

Stevens, 2015).

It had been previously thought that RCE above a horizontally homogeneous surface would produce quasi-homogeneous patterns of cumulus convection. However, Cloud Resolving Models (CRMs) and GCMs have shown that randomly distributed convection can cluster, or self-aggregate, into localized regions without any external drivers (Bretherton et al. (2005), Coppin and Bony (2015), Muller and Held (2012), Wing and Emanuel (2014), among others). Coppin and Bony (2015) proposed that for SSTs of ∼300 K, or close to current observations of SST, dry regions where low clouds reside radiatively cool effectively to space through the transparent upper atmosphere while simultaneously suppressing convection in this region. ds emit at a low temperature, which further decreases atmospheric LW cooling and generates a positive feedback. At SSTs greater than 305 K and less than 310 K, convective aggregation is initiated through strong surface winds formed in moist, convective regions that invigorate updrafts through surface fluxes induced by latent heating, instead of the shallow circulation mentioned previously (Coppin and Bony, 2015). Dry regions do not have such strong winds nor large surface fluxes to create an environment favorable for convection to occur.

Studies using RCE models suggest that convective aggregation can alter the moisture of the atmospheric state through a decrease in relative humidity in the upper troposphere (Bretherton et al., 2005, Wing and Cronin, 2016). As convective aggregates, there is an increase in humidity variance, implying that the moist columns' relative humidity increases despite the dry, clear regions decreasing in relative humidity (Wing and Emanuel, 2014). Precipitation efficiency increases in the moist columns, which, coupled

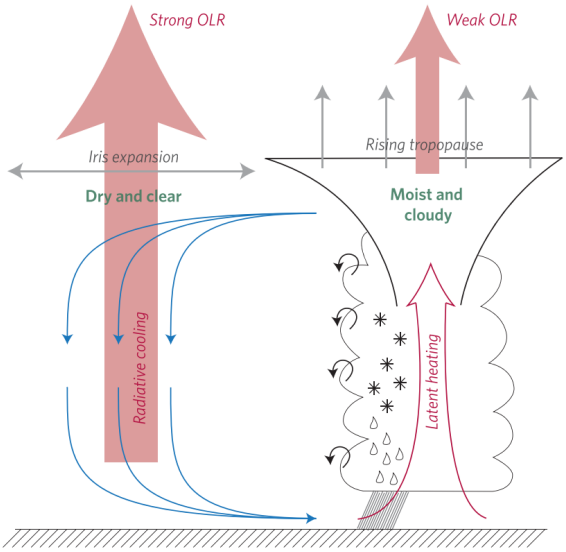

FIGURE 1.5: Illustration depicting the tropical atmospheric circulation between expanding dry, clear regions and suppressed moist, cloudy regions (Mauritsen and Stevens, 2015).

with an increase in upper tropospheric warming and a decrease in high clouds, has been shown to influence large-scale circulation and radiative heating in CRMs and GCMs (Coppin and Bony, 2015, Wing and Cronin, 2016).

Radiative-convective feedbacks are largely driven by radiative perturbations from extensive anvil clouds (Nilsson and Emanuel, 1999); thus, the net effect of aggregation depends critically on the relative magnitudes of its impact on SW versus LW radiation. A significant decrease in anvil fraction with warming could contribute a cloud feedback by either enhancing LW radiative cooling (Bony et al., 2016, Bretherton et al., 2005), or by decreasing SW reflectivity. Wing and Cronin (2016) found that reflected SW didn't change with aggregation due to an increase in low-cloud fraction with aggregation. This, in combination with an increase in OLR due to reduced anvil fraction, would result in a net loss of radiation at the top of the atmosphere (Wing and Cronin, 2016).

Infrared cloud observations of large-scale convective organization can be used to understand how convective aggregation can be applied to the real world, and what the potential radiative and precipitation responses are. Tobin et al. (2013, 2012) observed how convective organization behaved with the atmospheric state using satellite observations over the warm tropical ocean. They used the product between the normalized number of convective cores (N) and distance between them (D_0) to calculate the "Simple Convective Aggregation Index" (SCAI). For a given precipitation rate and domain, as the aggregated system increased, the precipitable water and relatively humidity decreased, which agrees with many modeling studies showing that the atmosphere dries in a more aggregated state. Tobin et al. (2012) is in agreement with modeling studies that precipitation efficiency increases within the moist and cloudy regions as aggregation increases. They hypothesize that convective mass fluxes are protected by the surrounding clustered convective systems, which inhibit both entrainment with the environment and rain evaporation. Due to mass conservation, less condensate is detrained in the free troposphere, which would decrease the anvil extent.

Models and observations don't agree on how increased convective organization influences climate. Unlike the modeling studies that found that increased convective organization didn't change the SW radiative response, Tobin et al. (2012) found that SW TOA fluxes decreased, which offset the increase in OLR and resulted in a near-zero net TOA radiative budget change. Despite this near-zero change, TOA radiative heating distribution may change due to the individual changes in SW and LW effects, which could influence large scale circulation (Tobin et al., 2012). Modeling studies suggest

that determining what thermodynamic processes are required for generating organized convection with thick versus thin anvils, as well how large-scale circulation influences these mechanisms, are crucial for determining the radiative impacts (Bony et al., 2006, 2004).

1.5 Research Objectives

This research approach contributes to understanding atmospheric convective behavior over ocean and the radiative responses in varying large-scale dynamical environments. Cloud, precipitation, and radiative flux products from the Afternoon (A-Train) satellite constellation and Pathfinder Atmospheres-Extended (PATMOS-x) cloud retrievals are used, as well as meteorological variables from reanalyses. The dataset features collocated observations from CloudSat, CALIPSO, AMSR-E, GOES, Meteosat, and MERRA using estimates of cloud center of gravity (COG), cold anvil area, precipitation intensity, SW, LW, and Net CREs in differing vertical pressure velocity regimes.

The main question that we seek to address is: **How does convective organization influence the link between precipitation and Earth's energy budget?** This question can be broken down into three subsequent questions:

1. How do the physical characteristics and radiative responses of convective systems vary with environmental conditions? (E.g., how big are convective cores?)
2. How does differing convective intensity influence convective behavior for a given dynamical environment? (E.g., does anvil area shrink with increasing convective intensity?)

3. How does differing convective intensity influence SW, LW, and net cloud forcings for a given dynamical environment? (E.g., is the SW or LW effect dominant in certain regions?)

This study is designed to leverage the strengths of A-Train observations in the context of broader swath and higher temporal resolution geostationary data supplied by PATMOS-x to explore the behavior of convection under varying dynamical regimes. An improved understanding of the links between large-scale circulation, convection, and climate are expected to lead to a more realistic representation of convective parameterizations in GCM simulations.

Chapter 2

Datasets and Methods

2.1 Introduction

This study was concentrated over the tropical North Atlantic Ocean, defined as 0°-35°N and 10°-80°W and highlighted in Figure 2.1. A database of physical and radiative characteristics of convection over the ocean were computed using A-Train, PATMOS-x geostationary, and MERRA reanalyses collocated datasets between 2007-2010. These values were calculated and averaged for every CloudSat swath that passed over 10°×10° grid boxes in the tropical North Atlantic Ocean. Results in Chapter 3 have computations over land omitted to decrease land's influence on convective systems—in other words only ocean-to-ocean comparisons were made. Figure 2.2 shows the ocean-only domains used for our study.

This chapter focuses on introducing the datasets and variables that characterize the behavior of convection over the ocean, which include the total number of deep convective cores that CloudSat identifies, the mean convective cloud's center of gravity

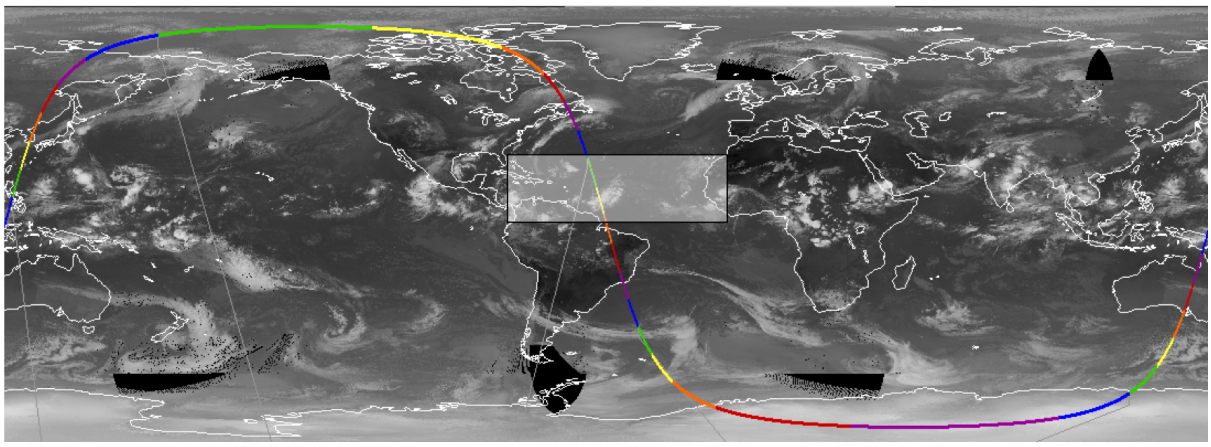

FIGURE 2.1: The orbital path for CloudSat granule 17771, obtained on August 30, 2009 and superimposed on global infrared satellite imagery. The highlighted region is the tropical North Atlantic Ocean—defined as 0°-30° N and 10°-80° W. The yellow line within the highlighted region corresponds to the CloudSat overpass shown in Figure 2.11.

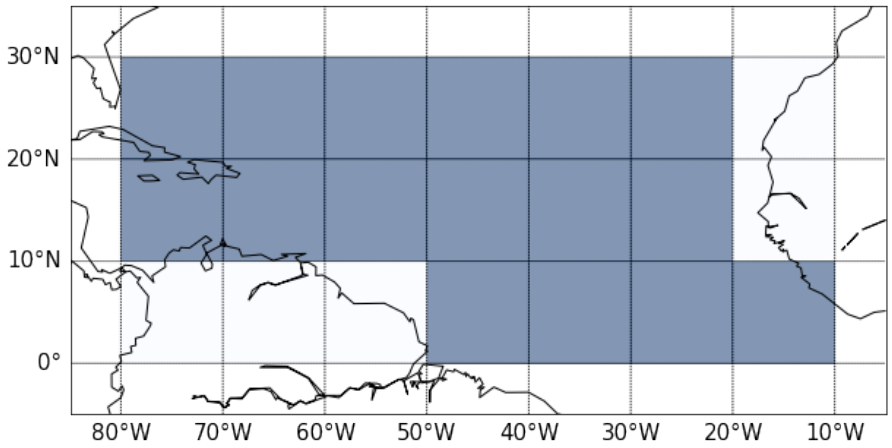

FIGURE 2.2: Map showing the 10°×10° ocean-only grid boxes shaded in grey.

(CoG) calculated with CloudSat's reflectivities, mean cold cloud area from PATMOS-x CTTs < 235 K, and conditional mean rain rates using AMSR-E rain rates. The radiative responses of convection over the ocean are also considered and presented in the form of SW, LW, and net CREs calculated using upwelling and downwelling TOA fluxes from CloudSats 2B-FLXHR-LIDAR product. Maps of the tropical North Atlantic Ocean during the Northern Hemisphere winter or dry season of the Tropics (December, January, and

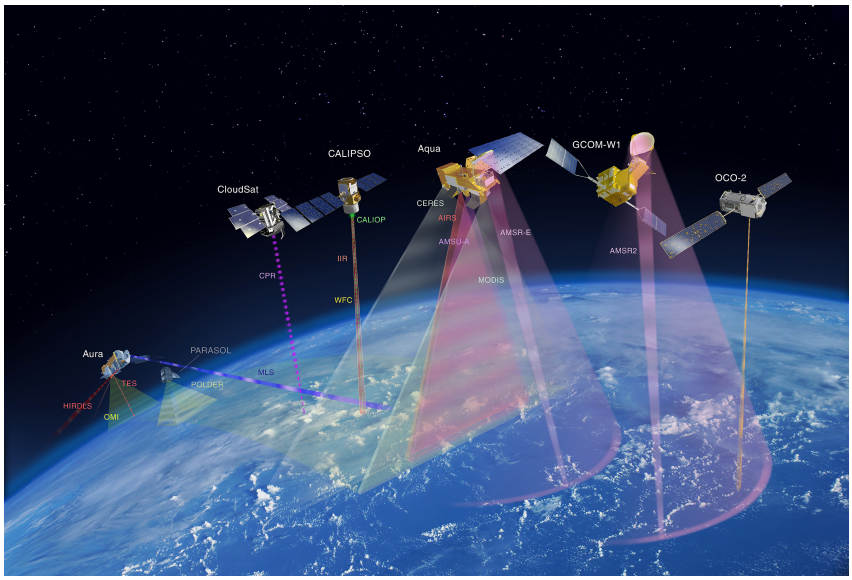

FIGURE 2.3: The Afternoon Constellation (A-Train) satellite mission with each satellite's instruments listed. Illustration courtesy of NASA.

February) are colored by each variable to show how the variable is distributed spatially with respect to large-scale circulation in the tropics.

2.2 The A-Train Satellite Constellation

Shown in Figure 2.3, the A-Train is a collection of satellites in sun-synchronous polar orbit crossing the equator in ascending direction at approximately 1:30 pm local solar time. Each satellite is within seconds to minutes of each other, which allows for near-simultaneous observations to be collected. It was created in 2006 when CloudSat and CALIPSO joined orbit with Aqua (launched in 2002), Aura (2004), and PARASOL (2004). The purpose of A-Train is to improved knowledge of clouds, aerosols, atmospheric chemistry, and other important variables crucial for understanding earth's climate and how it is evolving.

2.2.1 CloudSat

CloudSat was launched in 2006 to provide observations, such as cloud abundance and structure, for improving understanding of clouds and their radiative properties. On board CloudSat is the Cloud Profiling Radar (CPR), which is the first millimeter wavelength, or 94 GHz, cloud radar, and is 1000 times more sensitive than weather radars—allowing it to observe cloud properties. CPR is a nadir-looking radar measuring the power backscattered by clouds as a function of distance from the radar, and outputs vertical structures of reflectivities. CPR can detect a minimum of -30 dBZ. CloudSat has an along-track sampling of 2 km, 500 m vertical resolution, and 1.4 km cross-track resolution. It's antenna size is 1.85 m and has a pulse width of 3.3 μs, with a dynamic range of 70 dB and calibration accuracy of 1.5 dB.

2.2.2 CALIPSO

The Cloud-Aerosol Lidar and Infrared Pathfinder Satellite Observation, or CALIPSO, provides new insight into the role that clouds and atmospheric aerosols play in regulating Earth's weather, climate, and air quality. One of the instruments on board CALIPSO is the Cloud-Aerosol Lidar with Orthogonal Polarization, or CALIOP, which is a two-wavelength polarization-sensitive lidar measuring backscatter. Combining measurements from CALIOP with information from passive infrared and visible imagers from the Imaging Infrared Radiometer (IIR) and Wide Field Campera (WFC) allows for high resolution of vertical structure and properties of thin clouds and aerosols. Examples of properties that CALIPSO measures are cirrus emissivity and particle size.

2.2.3 Aqua

Launched in 2002, Aqua gathers information about Earth's water cycle, such as evaporation from oceans, water vapor in the atmosphere, and water contributions from clouds, precipitation, soil moisture, sea and land ice, and snow cover. It also measures radiative energy fluxes and aerosols. On board Aqua are MODIS, AMSR-E, AIRS, CERES, and AMSU-A. AMSR-E, or Advanced Microwave Scanning Radiometer, is a twelve-channel, six-frequency, passive microwave radiometer. It measures brightness temperatures, and vertically and horizontally polarized measurements are taken at all channels. Its spatial resolution is from 5.4 km at 89.0 GHz to 56 km at 6.9 GHz, with a 1445 km swath and sampling interval of 10 km for 5-36 GHz and 5 km for 89 GHz. AMSR-E measures precipitation rate, cloud water, water vapor, sea surface winds, and sea surface temperatures. Aqua's near-simultaneous flight-time with CloudSat allows AMSR-E rain rates to be collocated with CloudSat's overpass, which is portrayed in the middle panel of Figure 2.5. The Moderate Resolution Imaging Spectroradiometer (MODIS) is a 36-band spectroradiometer that measures visible and infrared radiation for creating projects ranging from vegetation and land surface cover to cloud and aerosol properties.

Precipitation yield is characterized using AMSR-E's conditional mean rain rates (<rain rates>), which are the rain rates averaged over only regions where it is raining. <Rain rates> are calculated for convective regions only—i.e. along every swath within each $10^\circ \times 10^\circ$ domain that CloudSat detects deep convective cores. Figure 2.4 shows the map of the tropical North Atlantic colored by <rain rates> that were calculated for DJF from 2007-2010. Like Figures 2.7 and 2.12, this map corresponds well with ω_{500} because

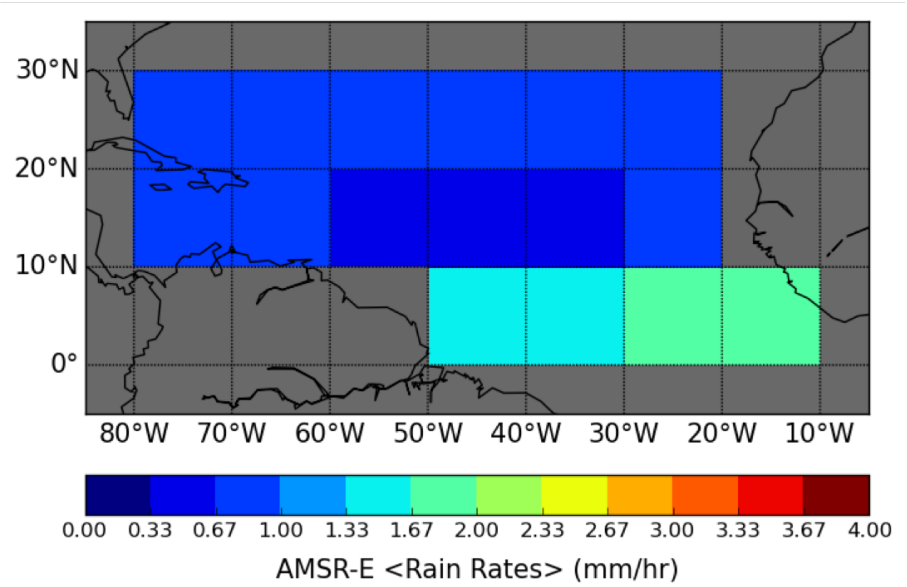

FIGURE 2.4: Map of the conditional mean rain rates from AMSR-E along CloudSat tracks for December, January, and February averaged from 2007-2010.

the highest rainfall rates are located in vertically ascending regions along the ITCZ. The ITCZ is largely responsible for much of the precipitation in the tropics, so we would expect precipitation yield to be larger in this region compared to subsidence regions.

2.3 CloudSat/CALIPSO cloud products

Measurements of the area of deep convective cores, intensity, precipitation yield, and radiative impacts of convective systems are supplied by CloudSat/CALIPSO cloud products. Within these cloud products are level-1b source data, which are calibrated data using pre-launch and in-flight calibration measurements. Level-2b and Level-2c are CloudSat standard and enhanced Level 2 data products, respectively, that contain derived geophysical variables at the same resolution and location as the Level 1 source data.

The 2B GEOPROF product supplies cloud-mask values that use information on the backscattering of cloud droplets to deduce if clouds have been detected. Another

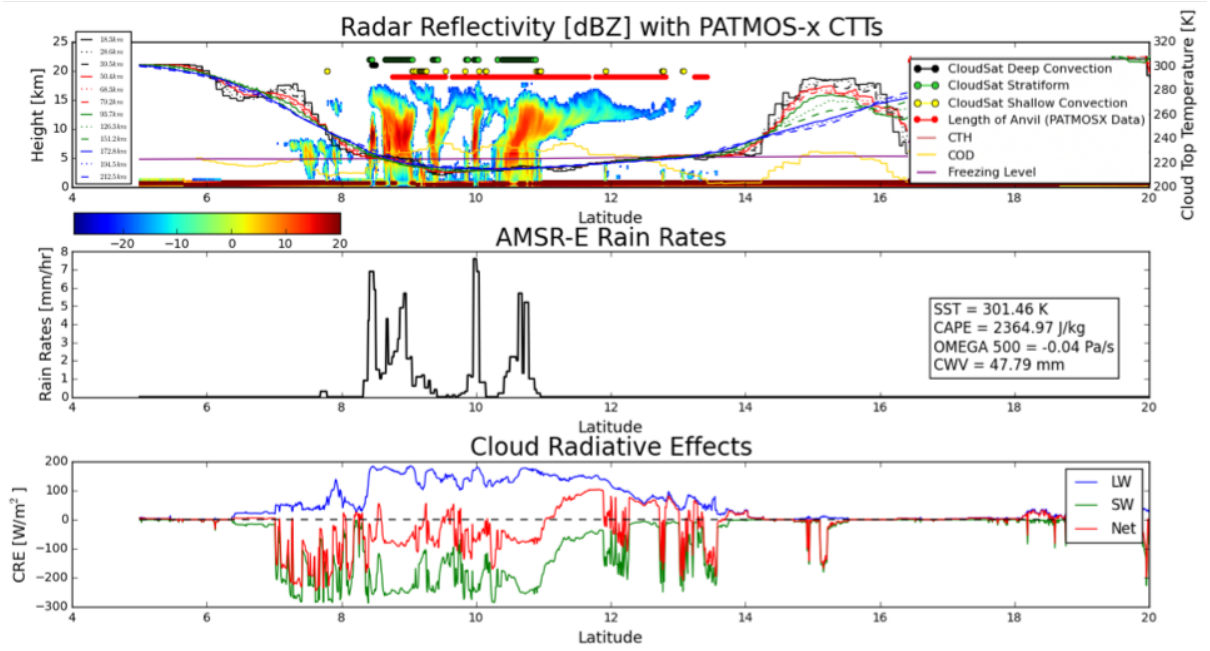

FIGURE 2.5: Data from August 30, 2009 (CloudSat granule 17771) are collocated and presented in three panels. Top panel shows CloudSat's CPR radar reflectivities with convective flags as dots. Middle panel has AMSR-E conditional mean rain rates with a box of mean values of MERRA-2 data supplying environmental context. Bottom panel shows SW, LW, and Net CREs.

measurement stored in 2B GEOPROF is the radar reflectivity, which is the calibrated measured return power proportional to droplet size to the sixth power (in units of dBZe = dB (mm^6 m^{-3})). These values are measured by identifying significant radar echo from hydrometeors for each vertical column that CloudSat samples. The highest radar reflectivity values correspond to the cloud systems' backscattering of the largest hydrometeors, as shown in the top panel in Figure 2.5.

Because CloudSat's CPR is highly sensitive to both solid and liquid precipitation, the signal is attenuated at the height where the largest hydrometeors are located (Smalley et al., 2014). Strong updrafts in convective precipitation can lift a significant

amount of liquid precipitation high above the 0°C freezing level, while stratiform precipitation is characterized by the presence of frozen hydrometeors above the freezing level, a melting layer about 500 m below the freezing level, and liquid precipitation below that. 2C-PRECIP-COLUMN makes use of the height of the attenuated signal to distinguish between convective and stratiform precipitation (L'Ecuyer et al., 2009). The height of attenuation is represented as an inflection point in CloudSat's vertical reflectivity profile and represents the top of the liquid precipitation in the column. If the inflection point height is more than 500 m above the ECMWF 0°C level then the pixel is flagged as convective–otherwise it is stratiform (L'Ecuyer et al., 2009). These flags are represented by the colored lines of dots in the top panel of Figure 2.5. When there are no reflectivity values equal to or greater than 0 dBZ above the freezing level, the pixel is classified as shallow convection. 2C-PRECIP-COLUMN also stores the height of the freezing level.

We are interested in understanding how differing environments influence the behavior of convection over the ocean—i.e., how does the strength and distribution of individual convective cells vary with large-scale circulation. One method for observing the distribution of convective cells is by physically counting how many convective cores there are within regions sorted by the strength of the vertical motion. The number of convective cores, defined by the CloudSat deep convective flag, were counted along every CloudSat footprint within each $10^\circ \times 10^\circ$ domain. Figure 2.6 shows how many convective cores CloudSat detected during DJF from 2007-2010. It doesn't seem like the average number of number of convective cores are dependent upon vertical motion. Yet, we should expect that the average number of convective cores is lower in the subsidence

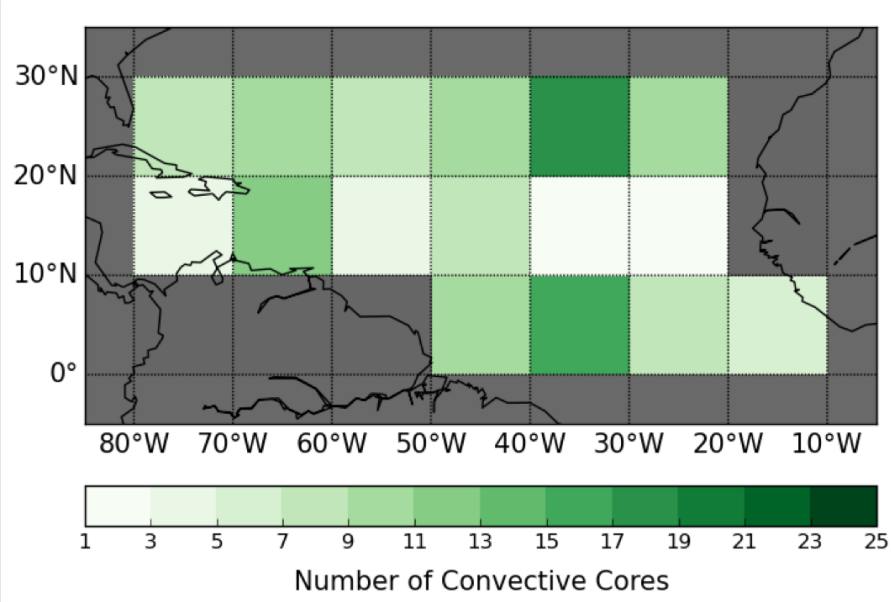

FIGURE 2.6: Map of the total number of convective cores along CloudSat tracks for December, January, and February averaged from 2007-2010.

region compared to the region of ascending motion (Igel et al., 2014).

In addition to characterizing how convection over the ocean is distributed, convective behavior can be characterized in terms of its intensity, horizontal area, and precipitation yield. A proxy for convective intensity is the deep convective cores' CoG. CoG is the height at which the mean weight of the cloud is located and is weighted by CloudSat's W-band reflectivities as noted in the following equation:

$$CoG = \frac{\Sigma_i Z_i H_i}{\Sigma_i Z_i} \tag{2.1}$$

where Z_i is the reflectivity and H_i is the height from the surface at the ith level in the atmosphere (Storer et al., 2014). This provides a direct measure of how high the largest hydrometeors are lofted into the atmosphere. Intensity is directly proportional to the CoG—i.e. the higher the CoG, the more intense the system.

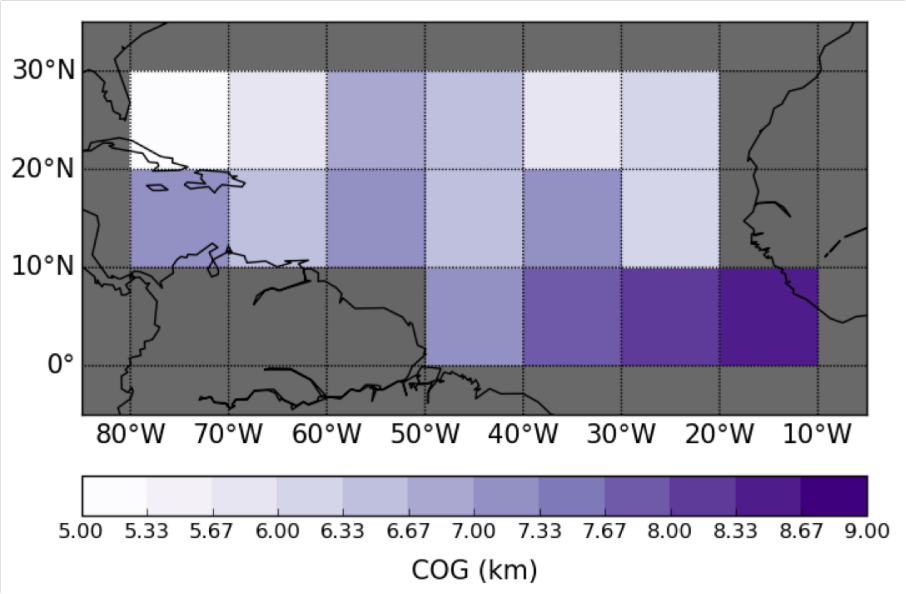

FIGURE 2.7: Map of the deep convective core center of gravity averaged along each CloudSat track and during December, January, and February of 2007-2010.

Figure 2.7 shows the mean CoG between 2007-2010 for DJF. The highest CoG values are located between 0°-10° N in which the ITCZ is located. Comparing it to Figure 2.13a and excluding grid boxes over land, the intensity directly corresponds to the strength of the vertical motion—clouds have higher centers of gravity in regions of strong ascending motion compared to regions of strong descending motion. This is understandable because rising motion allows hydrometeors to be lofted higher in the atmosphere than they would in regions of descending motion.

The 2B-FLXHR-LIDAR product supplies estimates of broadband fluxes and heating rates using CloudSat's CPR, CALIPSO, and MODIS measurements (Henderson et al., 2013). Upwelling and downwelling LW and SW fluxes are calculated using a broadband radiative transfer model for each radar profile supplied by CPR (L'Ecuyer et al., 2008). Flux calculations performed with clouds and aerosols removed are also

provided in the product. Using the TOA SW and LW fluxes in combination with the no-cloud flux values, SW, LW, and net CREs are calculated with the following equations:

$$CRE_{SW} = (F^{\uparrow}_{SW} - F^{\downarrow}_{SW})_{cloudy} - (F^{\uparrow}_{SW} - F^{\downarrow}_{SW})_{clear} \tag{2.2a}$$

$$CRE_{LW} = (F^{\uparrow}_{LW} - F^{\downarrow}_{LW})_{cloudy} - (F^{\uparrow}_{LW} - F^{\downarrow}_{LW})_{clear} \tag{2.2b}$$

$$CRE_{Net} = CRE_{SW} + CRE_{LW} \tag{2.2c}$$

where $F^{\uparrow}$ and $F^{\downarrow}$ are the TOA upwelling and downwelling fluxes with the respective wavelengths specified. The bottom panel of Figure 2.5 depict the SW, LW, and net CREs aligned with the CloudSat overpass. The designated anvil cloud area shows that the LW CRE is greater than zero, meaning that the LW component of the cloud's radiative response contributes to a warming effect. The same anvil area increases the magnitude of the SW response, resulting in a cooling effect. The net radiative contribution from the anvil area varies between positive and negative along the CloudSat overpass, which is most likely due to the anvil's varying microphysics and thus optical depth.

Establishing how convective organization influences radiation is done through observing the SW, LW, and net CREs calculated using the CloudSat/CALIPSO radiative flux product, as shown by Equation 2.2. Because CloudSat passes over every region only once a day (1:30 LST), the measurements are inaccurate portrayals of solar irradiances received by the tropics throughout the day. At 1:30 LST, the amount of sunlight that Earth's surface is near maximum, so the magnitude of the measured solar irradiances and resulting SW CREs are too large if these values aren't normalized to take into account

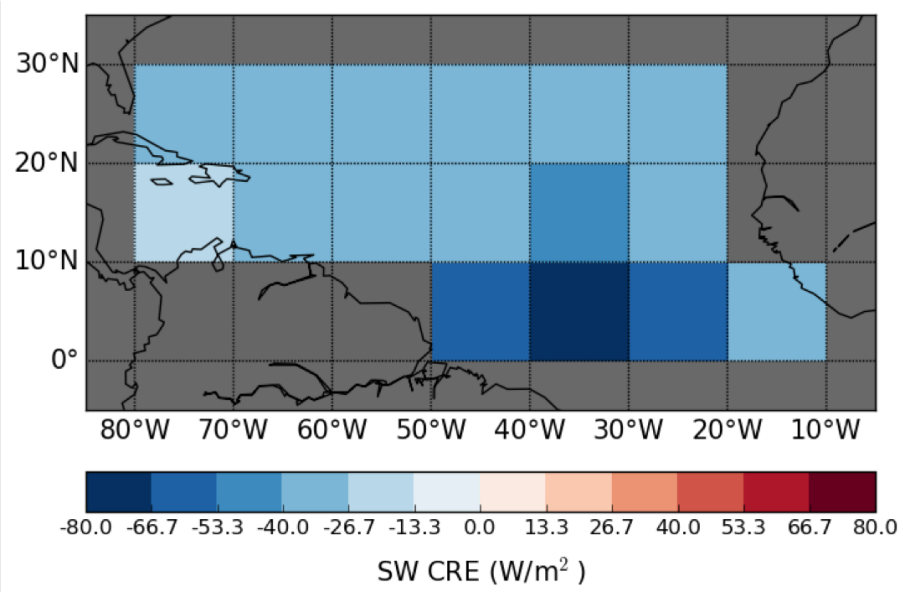

FIGURE 2.8: Like Figure 2.7 but showing shortwave cloud radiative effects.

the sunlight for the rest of the day. Seeing that solar irradiance isn't measured during CloudSat's nighttime tracks, we didn't calculate SW, LW, and net CREs using CloudSat's nighttime track measurements.

Figure 2.8 is a map of the tropical North Atlantic colored by daytime SW CREs that were averaged for every convective system that CloudSat detected within 10°×10° grid boxes during DJF of 2007-2010. SW CRE is most negative, or most dominant, along the ITCZ, or in regions of strong vertical ascent, which means that this region has a larger cooling effect compared to the subsidence regions.

A DJF map of daytime LW CREs are shown in Figure 2.9. Like the SW CREs, the LW radiative impact is most dominant along the ITCZ compared to the subsidence regions, which means that there is a larger warming impact coming from the vertically ascending regions than from the descending regions. The grid boxes that have the largest LW CRE also have the largest cold cloud area, which is expected.

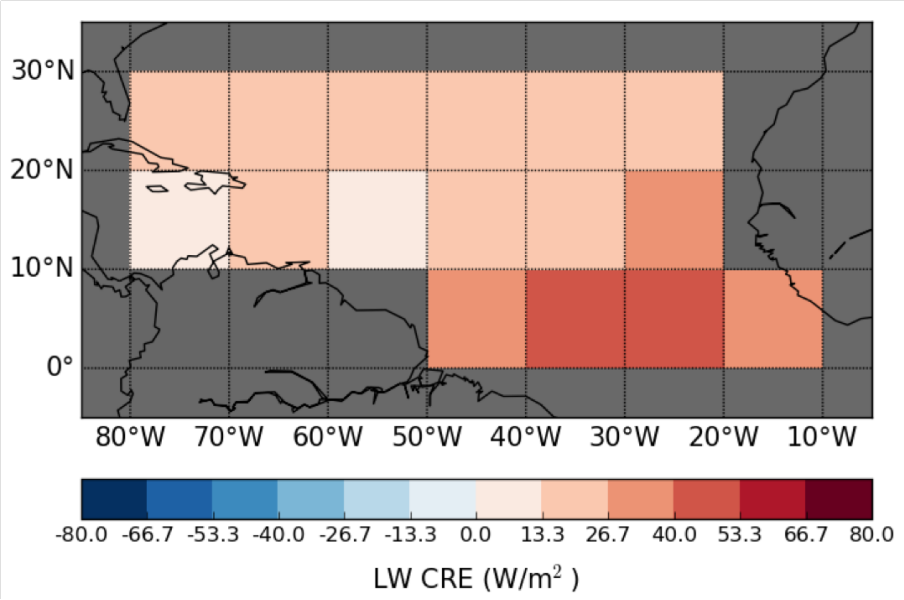

FIGURE 2.9: Like Figure 2.7 but showing longwave cloud radiative effects.

A map of the net radiative impact, which is the LW and SW CREs added together, by convective systems in the tropical North Atlantic is shown in Figure 2.10. Net CRE is negative meaning that the SW component dominates and implies that convective clouds have a cooling effect. SW CRE is slightly larger along the ITCZ compared to the subsidence regions, which implies that the convective systems found in the ITCZ have a marginally larger cooling effect than those found in the subsidence regions.

2.4 PATMOS-x

Cloud top temperatures from the PATMOS-x project supply spatial context for the deep convective systems detected by CloudSat. PATMOS-x is a satellite-based suite of cloud and aerosol products generated by both the National Oceanic and Atmospheric Administration (NOAA) and more recently the European Organisation for the Exploitation of Meteorological Satellites (EUMETSAT) Meteorological Operation satellite program

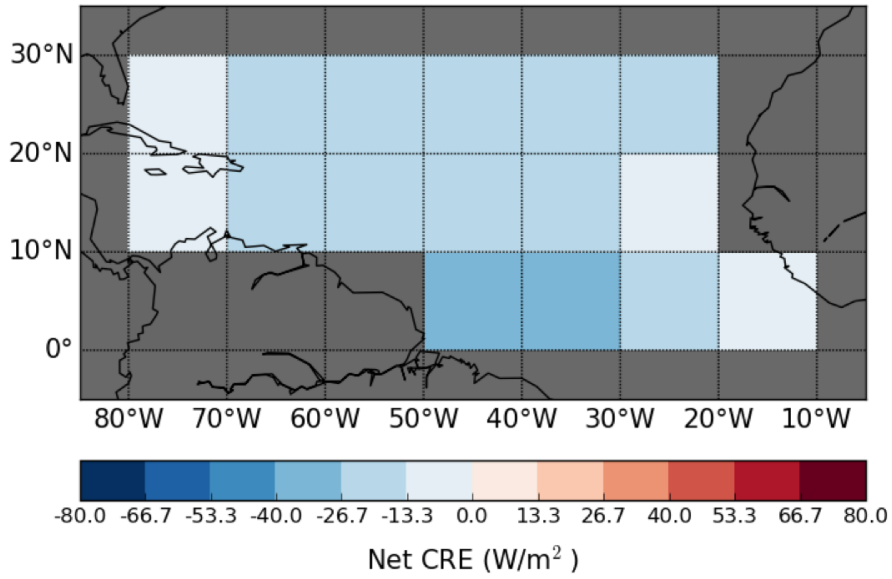

FIGURE 2.10: Like Figure 2.7 but showing net cloud radiative effects.

(MetOp) (Heidinger et al., 2012, Schmetz et al., 2002). The PATMOS-x record was initially generated from the Advanced Very High Resolution Radiometer (AVHRR) sensors flown on the NOAA polar orbiter satellite series and selected ancillary data since 1978 (Heidinger et al., 2014, Sun et al., 2015). It has since been generalized to produce cloud products from other instruments, including those on-board Geostationary Operational Environmental Satellites (GOES) and Meteosat Second Generation (MSG) (Foster and Heidinger, 2013).

This study takes advantage of geostationary data's broad spatial coverage and high temporal resolution by using PATMOS-x GOES-East (both GOES-12 and GOES-13) and MSG cloud datasets. Combining data from these satellites provides complete coverage of the tropical North Atlantic—0°-35°N and 10°-80°W with GOES-East spanning 40°-80°W and MSG 10°-40°W. GOES-12 and GOES-13 were positioned at 60°W

and 75°W, respectively, and provided twice-hourly full-disk scans with a spatial resolution of 4 km for infrared channels (Foster and Heidinger, 2013). Meteosat satellites are equipped with the Spinning Enhanced Infrared Imager (SEVIRI) that supplies continuous observations of the Earth using 12 visible and infrared channels.

PATMOS-x data provides level-1b files composed of sampled pixels, which allow for observations to be converted to radiances (Heidinger et al., 2014). A Bayesian cloud mask algorithm using collocated CALIPSO data has been developed for cloud detection and evaluation. This algorithm detects the AVHRR pixel closest to each 1 km CALIPSO cloud layer pixel and uses a nearest-neighbor approach for providing estimates of the collocated pixel for an entire global area coverage (GAC) orbit. The resulting hourly-pixel data is sampled and remapped to a $0.1^\circ \times 0.1^\circ$ grid (level-2b data) (Heidinger et al., 2014, Sun et al., 2015). With a probability of detection being at around 90%, it has been shown that this data set is in closer agreement with existing global cloud detection data sets compared to other passive satellite sensor data sets (Heidinger et al., 2012).

The cloud property of highest interest for this project is cloud-top temperature, but other cloud variables include cloud-top height and 11 μm cloud emissivity. These infrared cloud properties are derived using the ABI (Advanced Baseline Imager) Cloud Height Algorithm (ACHA), which uses an optimal estimation approach (Walther et al., 2013). ACHA runs in advance of the Daytime Cloud Optical and Microphysical Properties (DCOMP) algorithm, which is used for generating estimates of cloud optical thickness, cloud effective radius, and ice/water path during daylight (Heidinger and Pavolonis, 2009, Walther and Heidinger, 2012).

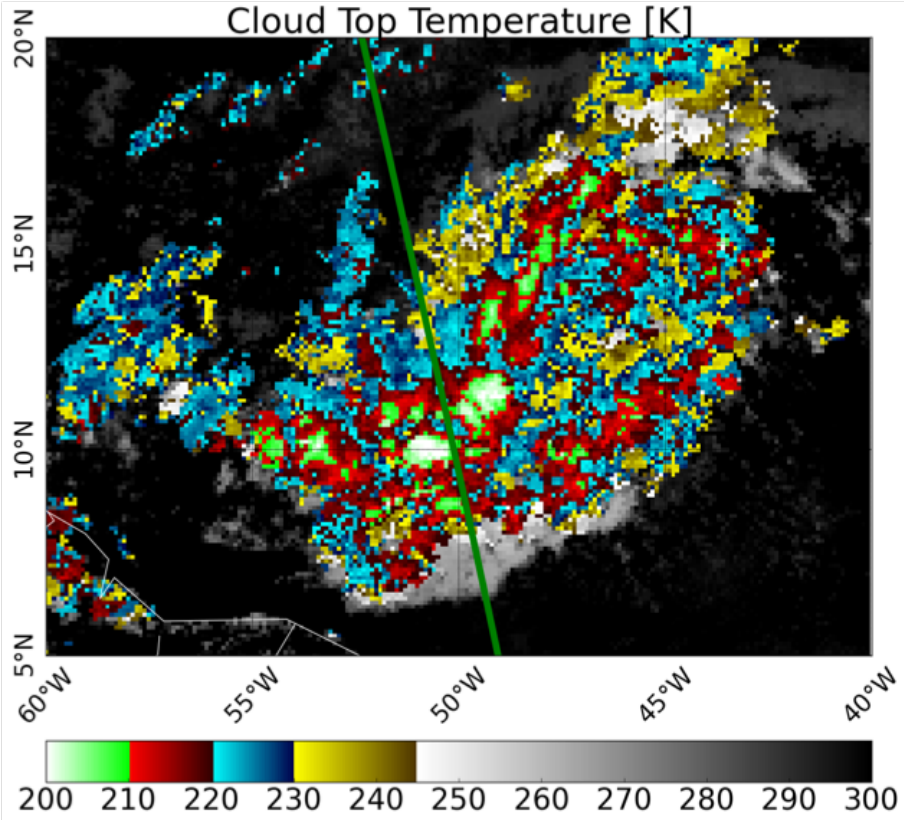

FIGURE 2.11: PATMOS-x satellite image from August 30, 2009 with cloud top temperatures from GOES-East shown in color. The green line is CloudSat granule 17771 showing that multiple cloud properties were simultaneously measured over the same region.

Figure 2.11 shows a snapshot of PATMOS-x cloud top temperatures supplied by GOES-East observations over a 15°N×20°W grid. The green line passing through the map is a CloudSat overpass, which demonstrates the feasibility of collocating observations from these two instruments. The CloudSat overpass in this figure is granule 17771, so the spatial mapping of cloud top temperatures provides background information to the reflectivity, precipitation, meteorological, and cloud forcing information depicted in Figure 2.1.

The area of convective systems is characterized by the fraction of CTTs < 235

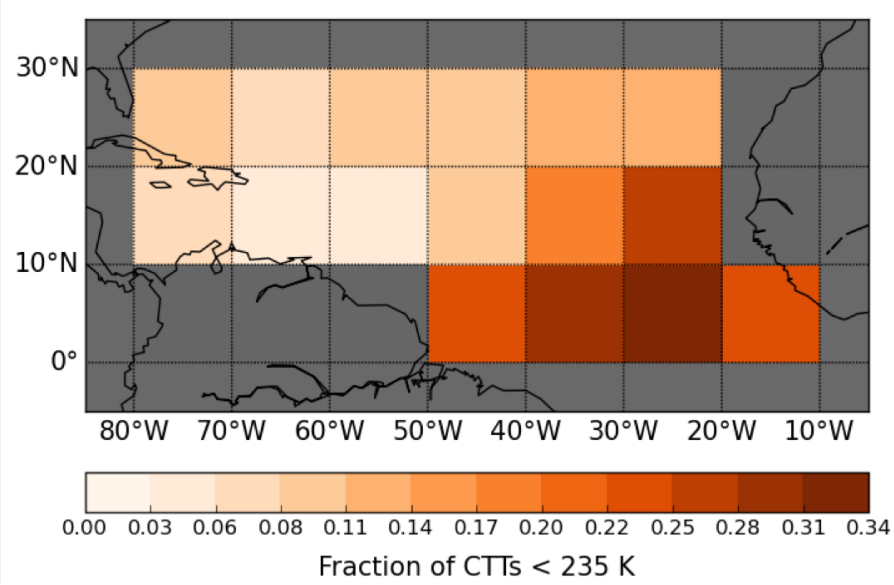

FIGURE 2.12: Like Figure 2.7 but showing fraction of cloud top temperatures < 235 K from PATMOS-x.

K, from the PATMOS-x cloud products, when CloudSat detected deep convection over the ocean within each $10° \times 10°$ domain. 235 K is chosen to take into account cold clouds, which includes both deep convective cores and the surrounding anvils (Arkin, 1979, Arkin and Meisner, 1987). Figure 2.12 is a map of the mean cold cloud area, given as the fraction of CTT $<$ 235 K within each grid box calculated at the times that CloudSat detected oceanic deep convection. As with CoG, cold cloud area's spatial variability is consistent with the spatial variability of vertical motion. The largest cold cloud areas are located along the ITCZ and smaller areas occur in the subsidence regions.

2.5 MERRA

The Modern-Era Retrospective analysis for Research and Applications (MERRA) reanalysis dataset was generated using the Goddard Earth Observing System Data Analysis System, Version 5 (GEOS-5) data assimilation system (DAS) (Rienecker et al., 2011). Its purpose is to improve how Earth's energy and water cycles are represented on both weather and climate scales by placing measurements from NASA's Earth Observing System (EOS) satellites into a climate context. MERRA's gridded resolution is $\frac{1}{2}^\circ$ latitude $\times$ $\frac{2}{3}^\circ$ longitude with 72 vertical levels from the surface to 0.01 hPa (Rienecker et al., 2008). Temporal resolution of the data ranges from hourly to monthly from 1979 to 2016. In 2016, MERRA-2, which is version two of MERRA, was introduced to take full advantage of the advances in its assimilation system—including assimilating observation types not previously available in MERRA.

A MERRA-AUX data product was created to store CloudSat-collocated MERRA variables, and was created before MERRA-2 came out. The collocation was performed by weighting MERRA values from the four nearest MERRA grid boxes to each of the CloudSat footprints. Of particular interest are the 2d MERRA-AUX variables characterizing the environment: vertical pressure velocity at 500 hPa (ω_{500}), CAPE, SST, and column water vapor (CWV). The middle panel in Figure 2.5 lists values for these variables that were averaged along CloudSat's track.

To observe how convection over the ocean responds in different environments, ω_{500} is used as a proxy for convection. Figure 2.13 are MERRA-2 ω_{500} maps for each of the

four seasons: December, January, and February (DJF); March, April, and May (MAM); June, July, and August (JJA); and September, October, and November (SON). We see that the strongest rising motion, or most negative vertical velocity, is predominantly located between 0°-10° N during DJF and MAM, which is when the ITCZ is located in the Southern Hemisphere. The ITCZ shifts north during JJA and SON, which we can tell by the large scale vertical rising motion that spans 0°-30° N between 80°-60° W. Additionally, large-scale subsidence is located at 0°-4° N in the eastern region of the tropical North Atlantic, and the ITCZ is shifted north about four degrees in this region as well.

Noting the predominant locations of large-scale rising and subsiding motion, we can also take a look at their distributions—e.g., is one type of motion more prevalent than the other? Figure 2.14a shows the cumulative distributions of ω_{500} where ω_{500} is averaged over every CloudSat swath within each grid box between 2007-2010. It is for the most part symmetric, with the cutoff for the top 25% rising motion being at approximately -0.03 Pa/s, and the top 25% descending motion being approximately 0.03 Pa/s. The mean is slightly offset in the positive direction from 0 Pa/s. Figure 2.14b shows a Gaussian distribution—the green curve—fit over the data.

The distribution of ω_{500} for when CloudSat detected oceanic deep convection is not symmetric, as shown in Figure 2.15. 0 Pa/s is the cutoff for the top 25% subsiding motion regime, meaning that 25% of the deep convection occurrences over the ocean were in either neutral or large-scale subsidence environments. For both Figures 2.14 and 2.15, most of the ω_{500} values are near-zero, meaning that the tropics and subtropics are largely

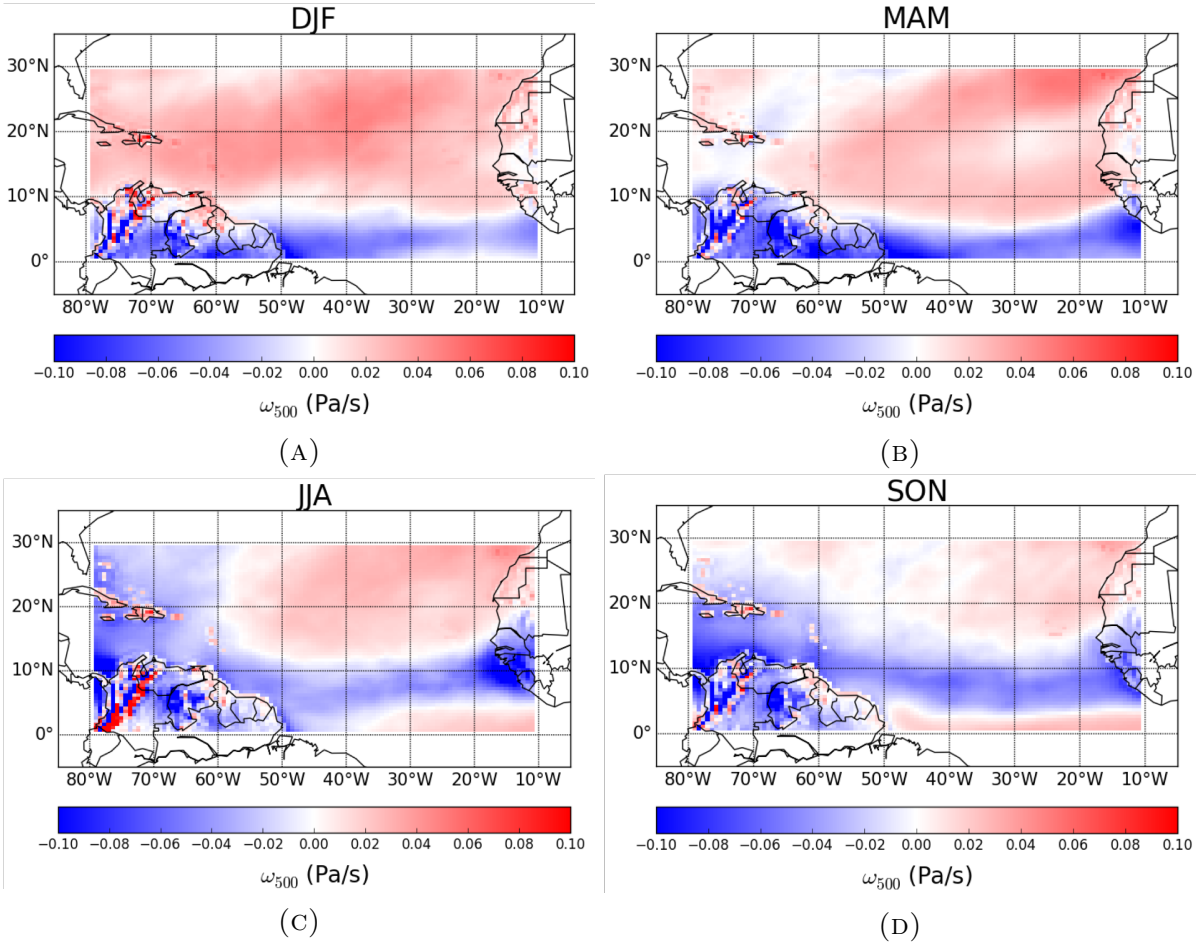

FIGURE 2.13: Maps of vertical pressure velocity for (A) DJF, (B) MAM, (C) JJA, and (D) SON

influenced by weak vertical motion. The clouds formed in regions of near-zero motion have a large radiative impact mainly because the near-zero motion is so prevalent, which was first noted by Bony et al. (2004). Yet, Bony et al. (2004) also found that deep convective and shallow systems in regions of large-scale ascent and descent, respectively, had substantial radiative responses such that they can't be ignored.

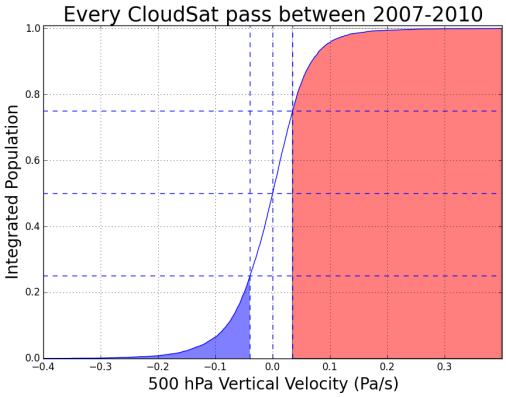

(A) CDF of ω_{500}

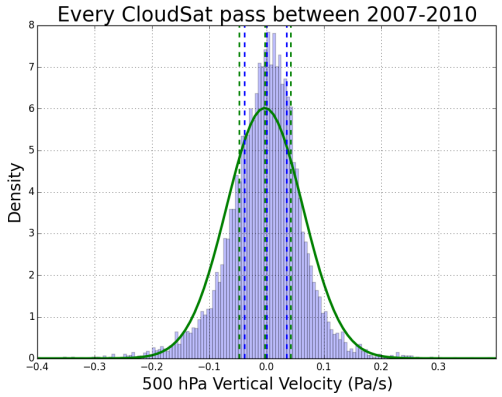

(B) PDF of ω_{500}

FIGURE 2.14: (A) CDF of ω_{500}. Top 25% rising (red shaded region) and top 25% descending (blue shaded region) motion are shown. (B) Histogram of ω_{500} in blue with a fitted Gaussian PDF in green. Quartile regimes (25%, 50%, 75%) for the data and fitted PDF are given by the blue and green vertical dashed lines, respectively.

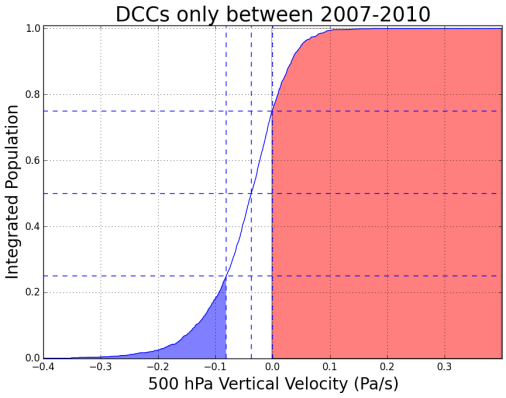

(A) CDF of ω_{500}

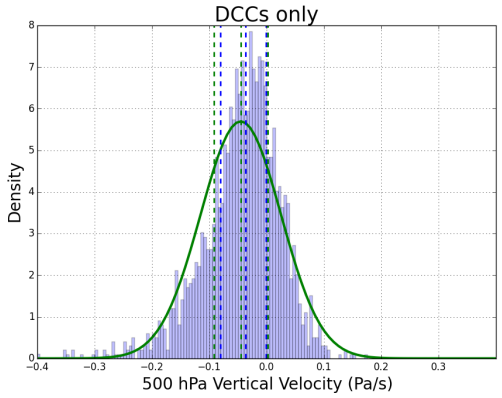

(B) PDF of ω_{500}

FIGURE 2.15: (A) and (B) are the same as in Figure 2.14 but show the distributions of ω_{500} only when CloudSat detected deep convective cores.

Chapter 3

Convective Behavior and Radiative Influence over the Tropical North Atlantic

3.1 Introduction

Studies show that the radiative budget in the tropics is influenced by changes in convective behavior induced by shifting large-scale circulation or changes in precipitation yield (e.g. Bony et al. (2015), Daloz et al. (2018)). This work takes advantage of A-Train, PATMOS-x, and MERRA reanalyses collocated measurements to assess environmental influences on convective behavior over the ocean and their precipitation and radiative responses. The first subsection identifies convective behavior trends with increasing midlevel vertical pressure velocity, or increasing subsidence, that acts as a proxy for large-scale circulation. The next two subsections examine how the physical and radiative properties of convection change with intensity in different dynamical regimes, where

the dynamical regimes are defined as the top 25% rising and descending motions that we determined in Figure 2.14. In other words, the convective properties are sorted by vertical motion strength.

Results are displayed as hex-binned scatter plots with regression lines to detect the sensitivity between the relationships, as well as box-and-whisker plots for understanding their distributions. Points contributing to the hex-binned and box-and-whisker plots are variables averaged over every CloudSat swath that identified convection over the ocean—except for number of deep convective cores and cold cloud area, which is the fraction of CTT < 235 K—within each $10^\circ \times 10^\circ$ domain shown in Figure 2.2.

3.2 Role of the Environment

3.2.1 Influence on Physical Characteristics

It is expected that as subsidence increases, the frequency that convection over the ocean occurs will decrease (Bony et al., 2004, Bony et al., 1997, Zelinka and Hartmann, 2009). Figure 2.15 shows how the number of convective cores change as a function of changing vertical motion. Distinguishing the spatial frequency of convective cores, we find in Figure 3.1 that the number of convective cores decreases with increasing subsidence—the means range from three cores for the stronger vertical ascent down to less than two cores for strong descent. Furthermore, the number of cores only changes when there is mean ascent ($\omega_{500} < 0$)—it does not change when there is mean descent.

From Figure 2.7, we show the spatial mapping of the intensity of storms, but how sensitive intensity is to environmental conditions is examined by plotting CoG versus ω_{500}

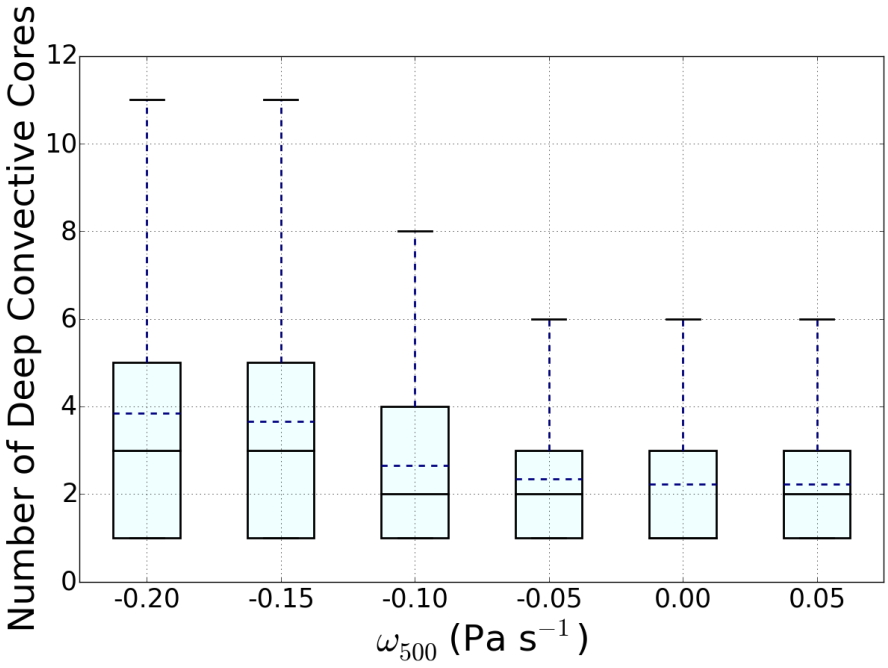

FIGURE 3.1: Box and whisker plot showing the mean (dashed line), median (Solid line), and interquartile range of the number of deep convective cores with ω_{500} that is averaged along CloudSat's track.

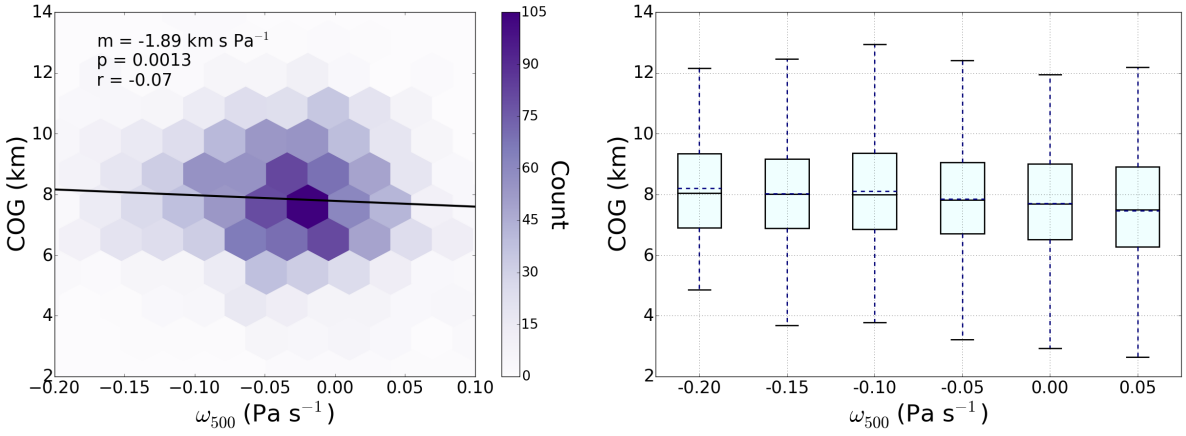

FIGURE 3.2: Hexbin (density) plot of deep convective cores' CoG averaged along every CloudSat swath varying with ω_{500}. Linear regression is given as a solid line and slope is given as m. B. Same as Figure 3.1 but for deep convective cores' CoG averaged along every CloudSat swath.

(Figure 3.2). As the flow becomes increasingly subsident, convective systems' intensity decreases, which is consistent with findings from Bony et al. (2004) and Igel and van den Heever (2015). We expect that as the flow becomes increasingly subsident, the vertical growth of convection is stunted (Bony et al., 2004). The regression line in Figure 3.2a suggests a weak negative relationship between CoG and ω_{500} with a correlation coefficient of r = −0.07. The regression line has a p-value of 0.0013, which is less than 0.05 meaning that the slope of -1.89 km s Pa^{-1} is statistically significant. To test the significance of the correlation coefficient, we use a t-statistic with a 95% confidence level and set the degrees of freedom as the number of unique days that CloudSat detects convection. The critical t is $t_{crit} = -1.86$, which is not less than $t_{0.025} = -1.96$, so the correlation is not statistically significant. Therefore, the null hypothesis that there is no relationship between CoG and ω_{500} is not rejected.

Igel and van den Heever (2015) also noticed a weak decline in convective intensity with ω_{500}—cloud top height only decreased by 1 km over a −0.5 Pa/s to 0.5 Pa/s range of ω_{500} (Igel and van den Heever, 2015). Figure 3.2b shows that the mean CoG hovers at around 8 km for every vertical velocity regime. As mentioned previously, most of the deep convective cores are concentrated in the −0.03 to 0.03 Pa/s vertical motion range, suggesting that convective systems tend to occur in weak vertical motion regions. The spread of CoG values is nearly consistent across the range of vertical velocity according to Figure 3.2b, despite the concentration of convective cores changing over the range.

The weak sensitivity between convective intensity and vertical pressure velocity suggests that there are other factors that could contribute to the variability of oceanic

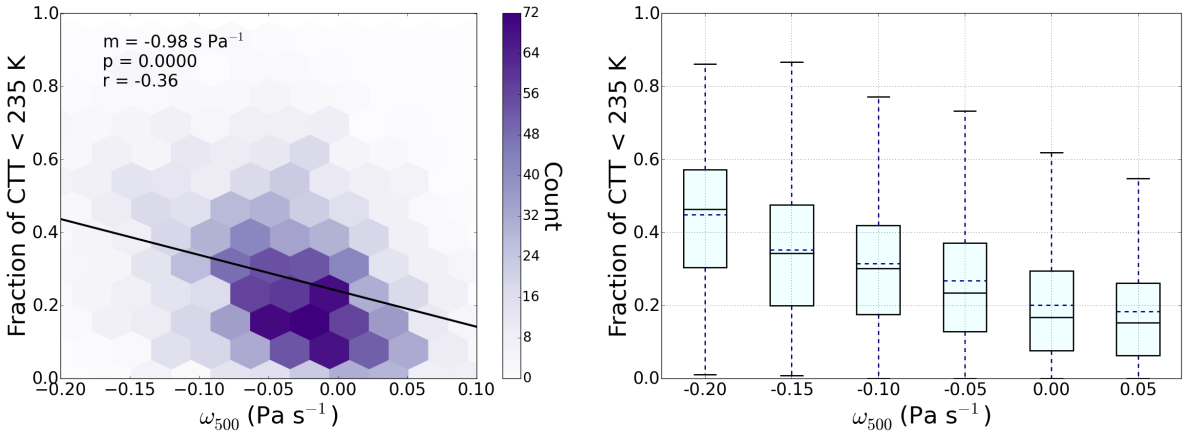

(A) (B)

FIGURE 3.3: A. Same as Figure 3.2a but for fraction of CTT $<$ 235 K averaged along every CloudSat swath. B. Same as Figure 3.1 but for fraction of CTT $<$ 235 K averaged along every CloudSat swath.

convective intensity for a given vertical motion. Vertical wind shear, the thermal stratification of the atmosphere, and the degree of the organization of convection are such factors that can vary with the same vertical motion (Bony et al., 2004). Although a weaker influence, SST could also impact the large spread in convective intensity (Bony et al., 2004).

In the previous chapter, we found that cold cloud area composed of both anvil and deep convective cores and defined as the fraction of CTT $<$ 235 K is strongly influenced by environmental conditions. To observe this relationship further, cold cloud area versus ω_{500} for deep convective regions over the ocean is shown in Figure 3.3a. The regression line depicts a decrease in anvil area—a fractional decrease of 0.98 over a -0.5 to 0.5 Pa s^{-1} vertical motion range—as subsidence increases. The p-value = 0, so the linear regression is statistically significant. For testing the correlation, we apply a two-tailed t-test with a 95% confidence level and set the degrees of freedom as the number of

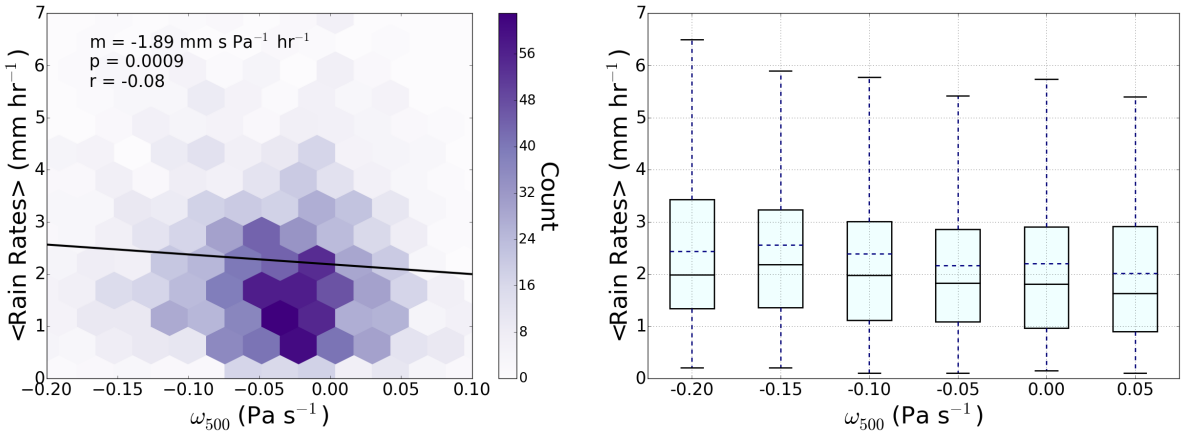

FIGURE 3.4: A. Same as Figure 3.2a but for <Rain Rates> averaged along every CloudSat swath. B. Same as Figure 3.1 but for <Rain Rates> averaged along every CloudSat swath.

unique days that CloudSat detects convection. We find that $t_{crit} = -9.78$, which is less than $t_{0.025} = -1.96$, meaning that the correlation coefficient of $r = -0.36$ is statistically significant. Vigorous updrafts have the potential to hinder hydrometeor fallout, and the amount of mass transported vertically and detrained is directly proportional to the upwards vertical velocity. It is therefore expected that cold cloud area increases with rising motion.

Igel and van den Heever (2015) found that the minimum mean anvil width occurs at 0.0 Pa/s and suggested that any magnitude of vertical velocity would cause anvil width to get larger. Yet, Figure 3.3b shows that the minimum in anvil fraction occurs when subsidence is greatest. The mean of cold cloud area decreases with increasing subsidence signifying that cold cloud area is highly sensitive to large-scale circulation.

We noticed in the last chapter that precipitation is more intense in regions of strong vertical ascent, which corresponds with the fact that convective systems along

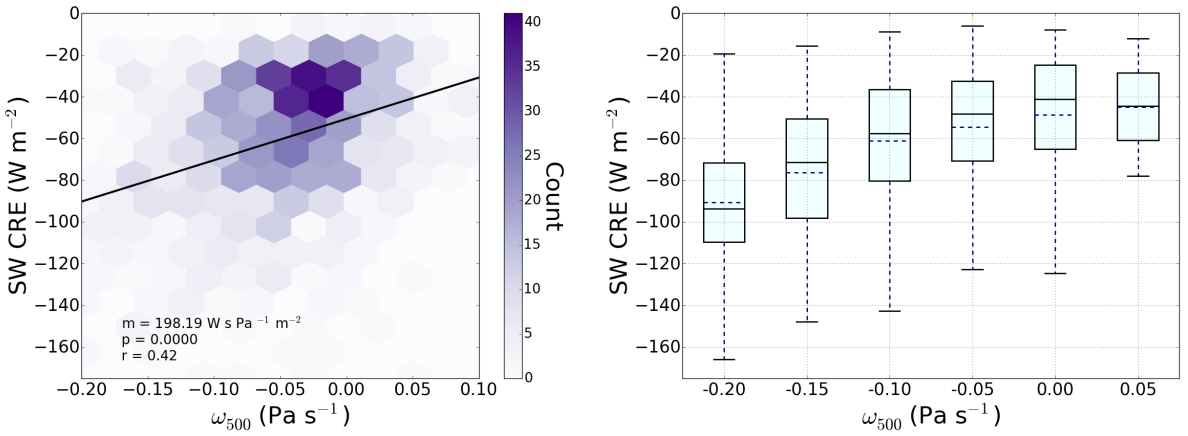

(A) (B)

FIGURE 3.5: A. Same as Figure 3.2a but for normalized SW CRE averaged along every CloudSat swath. B. Same as Figure 3.1 but for normalized SW CRE averaged along every CloudSat swath.

the ITCZ produce most of the precipitation in the tropics. The extent that large-scale circulation influences rain rates in regions that it is raining is considered in Figure 3.4. Following the linear trend line in Figure 3.4a, the strength of precipitation decreases by 1.89 mm s Pa^{-1} hr^{-1} over a -0.5 to 0.5 Pa s^{-1} vertical motion range. The p-value of 0.0009 means that the slope is statistically significant.

There is a large spread in rain rates across all vertical regimes—except in the strongest subsidence regime—as noted in Figure 3.4b. The decrease in rain rates isn't as prominent as the decrease in cold cloud area with vertical velocity increase (increased subsidence), which is further illuminated by the correlation coefficient, r = -0.08, that does not meet the 95% confidence level. Precipitation can be a proxy for convective intensity (e.g., Tobin et al. (2012)), so it follows that both CoG and conditional mean rain rates aren't depicting a strong sensitivity to varying environmental conditions, except for the strong subsidence regime where both precipitation and intensity drop substantially.

3.2.2 Influence on Radiative Characteristics

Because cloud radiative impacts are inextricably linked to precipitation efficiency—defined as how effective cloud condensate is converted to surface precipitation—(Bony et al., 2015, Stevens and Bony, 2013), we expect that cloud radiative effects will vary with environmental conditions much like precipitation yield does. We previously noticed that convective systems in the regions where strong vertical rising motion and highest precipitation yield occur have a larger SW effect—i.e. larger cooling effect—than in subsidence regions. Looking at Figure 3.5, we find that the magnitude of SW CRE decreases with increasing subsidence, showing a 200.15 W m^{-2} decrease over a -0.5 to 0.5 vertical motion range. This relationship, designated by r = 0.42, is significant to the 95% confidence level, which implies a strong cooling effect by convective systems in regions where vertical updrafts dominate that lessens as updrafts weaken or go away. The cooling effect is weakest where downdrafts are dominant. Figure 3.5b shows a large spread in SW CRE for environments with semi-strong updrafts (-0.30 $\rightarrow$ -0.1 Pa s^{-1}), but the spread decreases as vertical motion becomes more positive.

In Figure 2.9, we saw that LW CRE is largest along the ITCZ, implying that convective systems in this region have a strong warming effect in addition to the aforementioned strong cooling effect. Much like the SW component, the LW effect by convective systems is smaller in subsidence regions than in regions of strong ascending motion. These trends are noticeable in Figure 3.6a which shows that the magnitude of LW CRE decreases with increasing subsidence—by 169.08 W m^{-2} over a -0.5 to 0.5 Pa s^{-1} vertical motion range, and the sensitivity of LW CRE to vertical motion is statistically significant

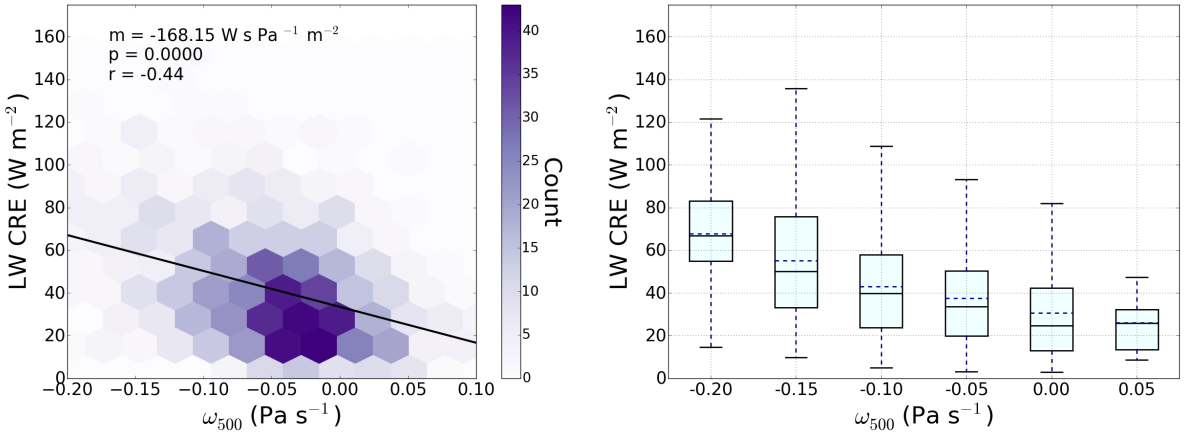

FIGURE 3.6: A. Same as Figure 3.2a but for daytime LW CRE averaged along every CloudSat swath. B. Same as Figure 3.1 but for daytime LW CRE averaged along every CloudSat swath.

to the 95% confidence level. The convective cloud's LW radiative influence is most closely associated with the cold cloud area for each range of vertical motion. As cold cloud area increases, clouds both emit at a lower temperature than Earth's surface and also have absorption properties that lessen the radiative cooling from Earth's surface. Hence, an increase in cold cloud area, which is found in the strong vertical ascent regimes, increases LW CRE and has a warming effect.

Both the tropics and the subtropics exhibit sufficient SW and LW radiative components that when combined can contribute towards a feedback. Figure 3.7 shows the general trend and spread in net CRE with vertical motion. Net CRE is negative across the range of vertical motion, which shows that convective systems have a cooling effect. The trend line shows net CRE slightly increasing with increasing subsidence, yet the shortwave and longwave effects nearly cancel each other out such that the relationship of net CRE to a change in vertical motion is not statistically significant.

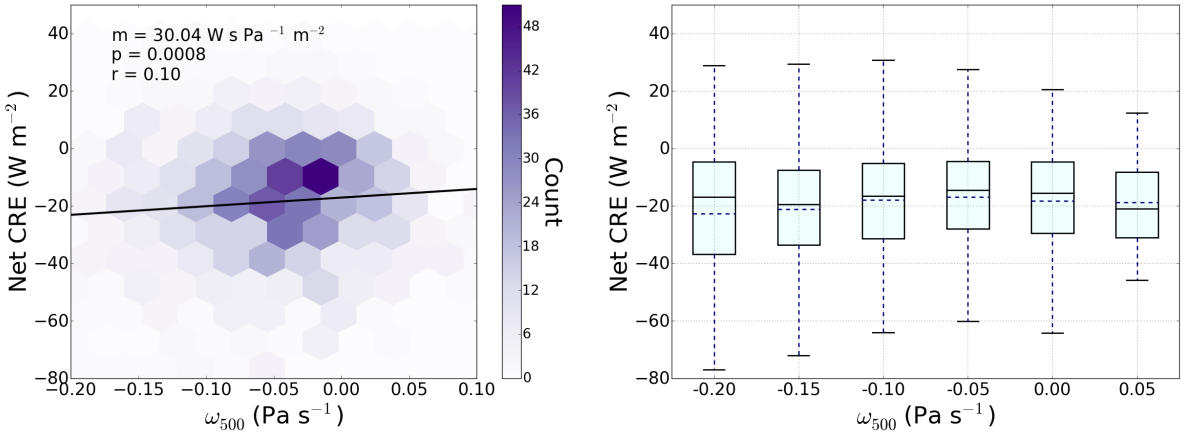

(A) (B)

FIGURE 3.7: A. Same as Figure 3.2a but for daytime net CRE averaged along every CloudSat swath. B. Same as Figure 3.1 but for daytime net CRE averaged along every CloudSat swath.

As mentioned previously, vertical motion doesn't have a large impact on CoG or rain rates, but it does strongly influence cold cloud area. As cold cloud area decreases, there is a strong decrease in SW reflectivity, which points towards a few different scenarios for how convection over ocean behaves for differing vertical motion strengths. One possible scenario is that cold clouds are sufficiently and equally optically thick or "bright" across the range of vertical motion to have a stronger SW radiative impact than LW radiative impact. The reason for net CRE becoming less negative as vertical motion becomes more positive would be solely due to the decrease in cloud cover. Another, more realistic scenario is that cold cloud area is composed of a mix of thin and thick anvils with different SW reflective capabilities such that the reduction in cloud amount doesn't provide a complete picture for how convective behavior alters radiative impacts.

The points in the previous paragraph are further complicated when examining the interquartile range in net CRE with vertical motion (Figure 3.7b). The highest mean

and medians of net CRE occur where the magnitude of vertical motion is at minimum, and the mean and medians of net CRE decrease as the magnitude of vertical motion increases. In fact, the means and medians of net CRE are the most negative in the highest subsidence regimes, but the spread in values in those regimes is shifted towards less negative net CRE values, which causes the trend line in Figure 3.7a to have a positive slope.

3.2.3 Discussion

To answer our question on **how environmental conditions influence the physical and radiative properties of convective storms**, both intensity and precipitation yield only weakly decrease as vertical motion increases. This implies that the intensity and radiative impacts of the storms are highly variable while keeping vertical motion constant, and point towards other factors, such as thermodynamic and cloud microphysical influences, which could be contributing to the broad range in convective behavior. It could also be that our analysis is capturing storms during varying lifecycle stages, which we noted previously as there being drastically different behavior patterns and radiative responses during different lifecycle stages. Yet, there is a strong decrease in number of deep convective cores as well as cold cloud area with increasing subsidence. Furthermore, while precipitation yield can give insight into the cloud radiative forcings, the significant changes in LW and SW radiative responses may be most closely associated with the differences in cold cloud area.

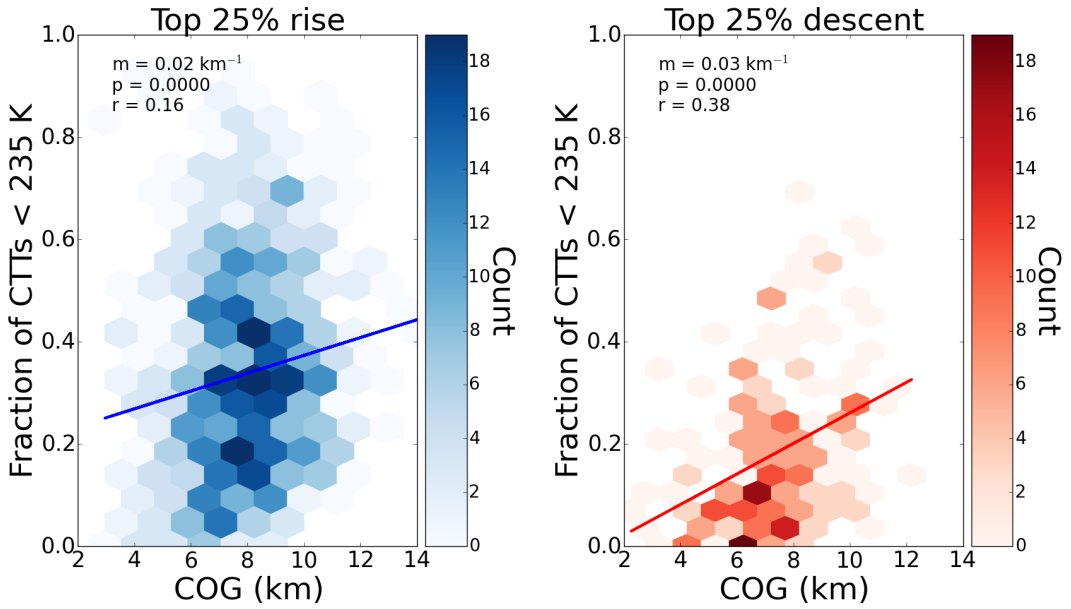

FIGURE 3.8: Density plots of PATMOS-x CTT < 235 K for every $10° \times 10°$ region that CloudSat detected a convective core between 2007-2010 varying with CoG in the (left) top 25% ascending motion regime and (right) top 25% descending motion regime.

3.3 Role of Convective Intensity

3.3.1 Influence on Physical Characteristics

To understand how precipitation and radiation are expected to change as storm intensity increases with climate, this next section will look at sensitivities between intensity and convective systems' physical and radiative characteristics. The relationships are sorted by the top 25% of vertical rising and subsiding motion to isolate the dynamical influences on convective behavior.

How changes in intensity influence cold cloud area can provide insight into the processes driving convective behavior. Figure 3.8 shows that in regions of strong vertical ascent and descent, cold cloud area increases with increasing convective intensity, and this relationship is significant to the 95% confidence level for both dynamical regimes. These

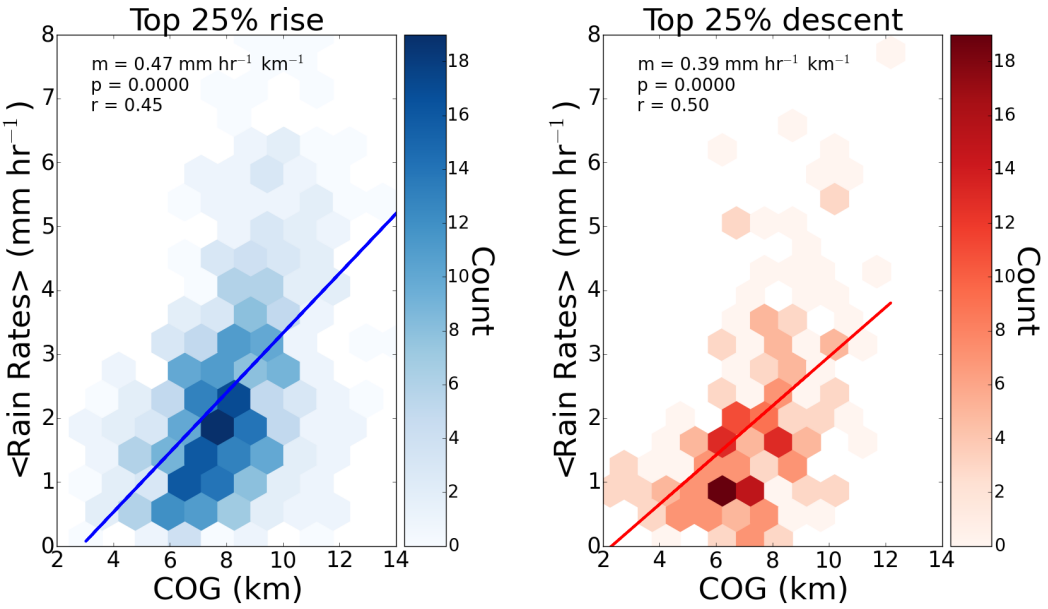

FIGURE 3.9: Like Figure 3.8 but for <rain rates> averaged along every CloudSat swath.

two variables are slightly more sensitive to each other in the regime of strong downdrafts, with a 0.03 fraction change in cloud cover per unit height increase in storms' CoG compared to the 0.02 fractional increase found in the strong ascending motion regime. But the difference between sensitivities is not very large, and is consistent with how intensity behaves in different environments. In regions where subsidence occurs, convective systems tend to stabilize the atmosphere and cause anvils to spread, which explains the increase in cold cloud cover as intensity increases. Convective systems across all dynamical regimes would have enhanced convective mass fluxes and detrainment as intensity rises. Yet, in the strong rising motion regime, the higher the convective intensity goes, detrainment isn't as favorable as it is in the subsidence region because the atmosphere is unstable, so clouds would tend towards rising as opposed to spreading.

We mentioned earlier that precipitation is often used as a proxy for convective

intensity, so we expect that precipitation and intensity are closely linked. Figure 3.9 shows that there is a statistically significant, to the 95% confidence level, increase in rain rates with convective intensity for both regimes—increasing by almost 0.5 mm/hr with each kilometer increase in CoG. Physically, this means that precipitation efficiency increases as convective intensity does, which is consistent with how precipitation is expected to behave with climate (Held and Soden, 2006). The increase in precipitation with convective intensity is only slightly stronger in the rising motion regime than in the strong descending regime—by 0.08 mm hr^{-1} km^{-1}. While we already noted that CoG and rain yield aren't individually largely sensitive to environment conditions, these results suggest that the relationship between these two characteristics only weakly depend on the environment.

3.3.2 Influence on Radiative Characteristics

RCE implies that changes in global mean precipitation are constrained by variations in atmospheric radiative cooling, so cloud radiative responses can be linked to changes in precipitation yield and frequency (Held and Soden, 2006, Stephens and Ellis, 2008). As precipitation increases with increasing convective intensity, the radiative responses could influence climate sensitivity by generating a feedback. To examine this idea, we analyze how a change in convective intensity influences the SW and LW cloud forcing components to understand how they contribute to the net radiative response. The following results show SW, LW, and net CRE varying with convective intensity sorted by the top 25% of vertical rising and subsiding motion to isolate the dynamical influences (Bony et al., 2004).

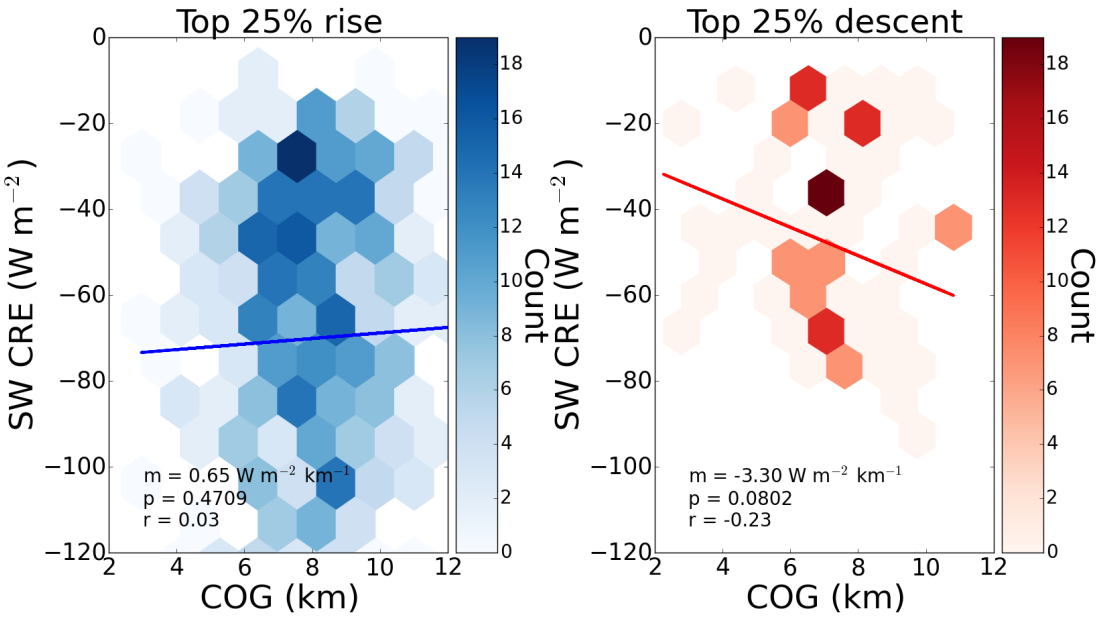

FIGURE 3.10: Like Figure 3.8 but for normalized SW CRE averaged along every CloudSat swath.

Figure 3.10 shows how SW CRE varies with convective intensity. The correlations between SW CRE and CoG on in both vertical motion environments are not statistically significant to the 95% confidence level despite there being seemingly opposite trend line behaviors between the two environments. For the ascending regions, it is likely that there is no relationship between SW CRE and CoG, or that the relationship is nonlinear. The descent case likely does not have enough data to determine a relationship.

Figure 3.11 depicts the behavior of LW cloud forcing with convective intensity. LW CRE increases with increasing intensity for both regimes, which makes sense given the cold cloud area increase with intensity for both regimes. However, the correlation between LW CRE and CoG are not significant to the 95% confidence level for either vertical motion environment. Thus, we cannot explicitly say that as convective intensity increases, the LW contribution from convective storms will have an enhanced warming

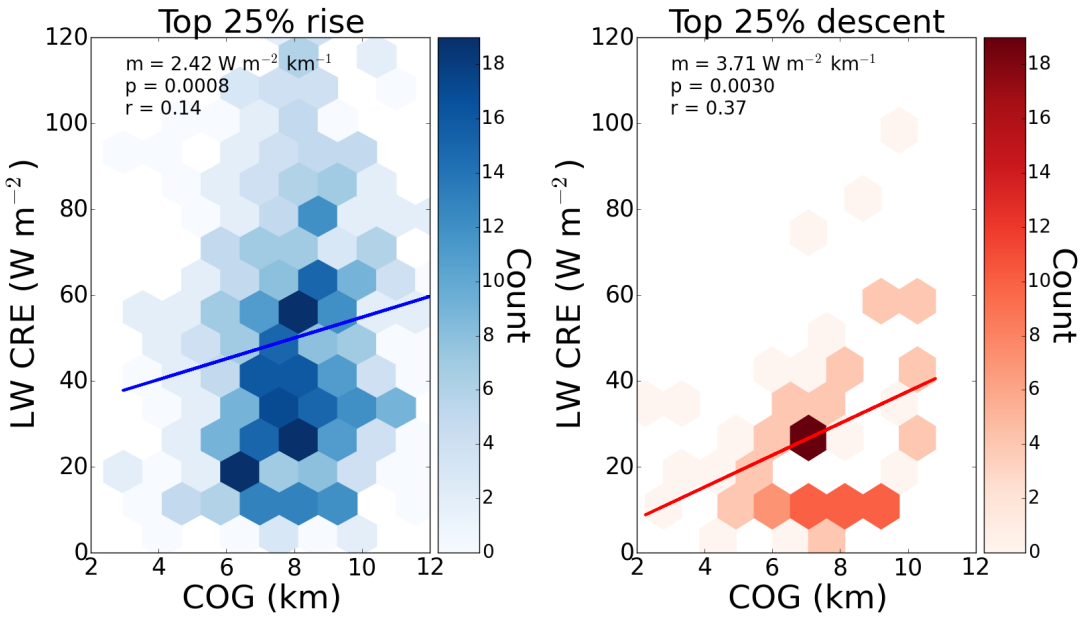

FIGURE 3.11: Like Figure 3.8 but for daytime LW CRE averaged along every CloudSat swath.

effect.

Combining SW and LW can give a clearer picture of the total radiative impacts than examining each one on their own. Fig. 3.12 shows that net CRE trend is negative for both regimes across all CoG heights, meaning that convective systems tend to have a cooling effect. Yet, in the rising motion regime net CRE increases by 3.07 W m^2 per kilometer increase in deep convective CoG, and the correlation is significant to the 95% confidence level. This trend arises from the slight decrease in magnitude of SW cloud forcing adding to the positive increase in LW forcing, which implies that the cooling effect weakens with convective intensity. It appears that this trend would be more positively steep if it weren't for a few largely negative net CRE outliers. This is opposed to the vertical descent environment in which the SW and LW effects nearly cancel each other out and net CRE is nearly neutral—the trend increases by 0.41 W m^2 per kilometer

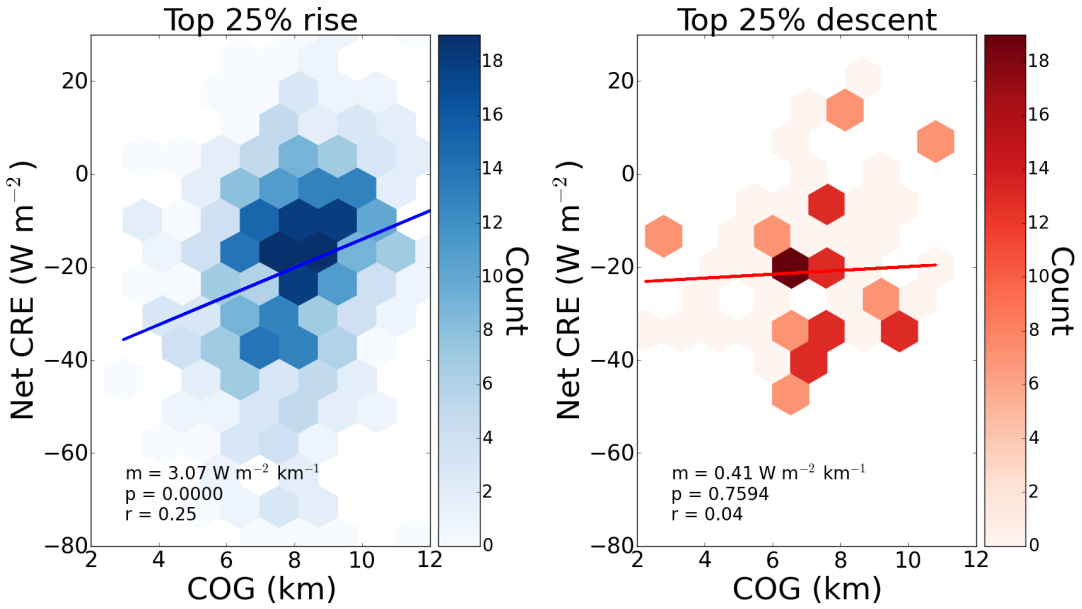

FIGURE 3.12: Like Figure 3.8 but for daytime net CRE averaged along every CloudSat swath.

increase in deep convective CoG as convective intensity increases. As a result of the shortwave and longwave effects canceling each other out, the correlation between net CRE and convective intensity is not statistically significant. The net CRE trend is less negative in the subsidence regime than in the rising motion regime for CoG heights up to about 8 km, which from Figure 3.2b is roughly the mean value of CoG for most of the dynamical regimes. If convective intensity is expected to increase with climate, the mean value of CoG will most likely rise and, according to these trends, could flip the sign of net CRE—resulting in a positive feedback.

3.3.3 Discussion

In answering **how do differing convective intensities influence convective behavior for a given dynamical environment**, we find that cold cloud area increases

with increasing convective intensity for both dynamical regimes, but that the sensitivity between these two variables is marginally larger in the strong subsidence regime. The strong relationship between precipitation and convective intensity is apparent in both regimes, but is noticeably stronger in the region of strong ascending motion. Precipitation yield increasing with convective intensity is consistent with current literature suggesting that precipitation efficiency is expected to increase in regions where convective intensity increases with climate change.

The question of **whether SW or LW cloud forcing is dominant in certain regions** can be answered by looking at how the SW and LW CREs add together to produce the net radiative impact. For both dynamical regimes, the SW component dominates and produces an overall negative net CRE across all intensities. The change in net CRE increases with intensity for the regions of ascending motion, which implies that the LW cloud forcing component becomes prevalent as intensity increases. However, in the subsidence regime the change in net CRE is nearly zero, meaning that the SW and LW effects nearly cancel each other. These impacts can be explained by understanding how convective morphology, such as cold cloud area, the distribution and size of deep convective cores, and precipitation amounts, evolve within differing dynamical regimes.

Chapter 4

Discussion and Future Work

This study combines observations from the A-Train constellation and PATMOS-x to study how convective behavior over the ocean and their radiative responses evolve under varying dynamical conditions supplied by vertical motion data. CTTs from PATMOS-x provides large spatial coverage, as well as high spatial and temporal resolution, to describe the cold cloud area created by convective updrafts. CloudSat's CPR complements these products with highly sensitive measurements of intensity to give insight on the relationships between convective intensity and the anvils that are generated. Combining these results with AMSR-E's, CloudSat/CALIPSO's, and MERRA reanalyses' rain, radiative flux, and meteorology data sets demonstrates the advantages of collocating observations.

4.1 Ties to Convective Aggregation

Results from this study provides physical insights into convective aggregation. CRM and GCM simulations and observations show that with increased convective organization, anvil cloud cover shrinks (e.g. Bony et al. (2016), Tobin et al. (2013, 2012),

Wing and Cronin (2016)). Assuming that with increased organized convection over the ocean there is an increase in convective intensity, and, therefore, CoG, we did not notice a decrease in anvil cloud cover; in fact, we found that as convective intensity increased, cold cloud area increased as well. An important note to mention is that studies show that a decline in anvil cloud cover is mostly influenced by an increase in SST (Bretherton et al., 2005, Coppin and Bony, 2015, Igel and van den Heever, 2015), which is a variable that we did not consider.

Studies suggest that as convection becomes aggregated, convective intensity and precipitation efficiency are supposed to increase in confined regions. Our results show that the size of convective cores and precipitation yield increase with intensity, affirming these previous studies. Our results also show that intensity and precipitation yield aren't highly sensitive to dynamical environments, which agrees with Igel and van den Heever (2015), so the precipitation response to increasing intensity is constant for all environments.

Radiative responses, however, are very much dependent upon environment conditions. In regions of strong updrafts, the SW effect is more significant than the clouds' LW forcing, but the LW contribution becomes more significant and SW becomes less so as intensity increases, which is noticeable in the negative net CRE that decreases in magnitude with increasing intensity. In regions of strong downdrafts, net CRE is negative and only marginally varies with an increase in intensity. There is, therefore, a larger radiative response to convective intensity in large-scale ascent compared to descent regimes. Without looking at different dynamical regimes, Tobin et al. (2012) and Tobin et al. (2013) noticed that net CRE of increased organized convection was near-zero due to SW and

LW effects cancelling each other, and suggested that despite the near-zero net CRE, the distribution of radiative heating in the atmosphere could be largely impacted because the distribution of convective organization is itself influenced. Our results further suggest that the difference in radiative responses between different environments could contribute to differentials in radiative heating at TOA, which could alter large-scale circulation and how cloud cover is distributed (Tobin et al., 2012).

4.2 Climate-scale Impacts

In addition to shifts in convective radiative responses that may impact large-scale circulation, as the Earth warms with climate change, tropical circulation is expected to weaken, which implies a weakening in the rate of total atmospheric mass transport (Bony et al., 2013, Chadwick et al., 2013, Merlis, 2015). This is consistent with the imbalance between an expected large increase in atmospheric water vapor following the Clausius-Clapeyron relation and a much slower increase in precipitation yield (Held and Soden, 2006, Stephens and Ellis, 2008). The ascent region of the Hadley cell dominated by the ITCZ is expected to narrow and weaken in transporting mass vertically, while its subsidence region is expected to expand (Lu et al., 2007), following the expected increase in radiative cooling in regions of descending motion (Knutson and Manabe, 1995, Lau and Kim, 2015). In addition to the narrowing and weakening in strength, the ITCZ's precipitation yield is expected to increase (Lau and Wu, 2007) and the ITCZ is projected to remain in the same location with climate change (Byrne et al., 2018).

Projected responses of the ITCZ to climate change are dependent upon the

net energy input to the atmosphere, as well as dynamical and thermodynamic processes responsible for transporting energy (Byrne and Schneider, 2016a,b). For the current climate, our results show that for weak ascending motion, convective systems decrease only slightly in intensity and precipitation yield, with a much stronger decrease in cold cloud area. Weakened ascending motion suggests that more investigation into the radiative impacts from convective systems in near-zero vertical motion regimes should be done. As is currently the case, convective systems in a weaker ascending motion regime have a smaller negative net CRE compared to systems in regions of strong ascent. The expanding subsidence region suggests that convective systems in subsidence regions could increase. Our results show that convective systems in subsidence regions are less vertically intense with smaller precipitation rates and cold cloud areas than convective systems in regions of ascent. The trend line in 3.7a suggests that net CRE becomes less negative as subsidence increases. It is important to note that our results do not reflect how convection will behave and contribute to Earth's radiative budget in a warming climate.

4.3 Limitations in Analysis

There are some limitations in our current analysis that should be addressed. The $10^\circ \times 10^\circ$ domain size is most likely too large for partitioning vertical velocity behavior into different regimes. This is evident in Figure 2.13 because the ITCZ doesn't expand 10° in latitude. Future work could involve splitting the Atlantic into smaller domains. Another way to resolve this issue, as well as a potential issue of splitting up storm systems using a fixed-domain method, is using a modification of the cloud-object identification method in

Igel et al. (2014): first identify the deep convective core using CloudSat's convective flag product, and then average variables within a certain designated region from the convective core. Each convective system and their associated physical and radiative characteristics would be sorted by vertical motion averaged over the cloud object only. "Clear objects" would also be defined, which includes characterizing clear sky between convective cores, so that we could relate to the convective aggregation theory.

Another drawback to our current analysis is that CloudSat overpasses most likely misses large storm systems that PATMOS-x detects because of PATMOS-x's large spatial coverage, which could possibly be creating a sampling issue and might be skewing the relationship between convective intensity and cold cloud area. Taking advantage of CTT < 195 K from PATMOS-x could be useful for identifying the convective cores that CloudSat misses.

4.4 Future Work

The focus of this study takes into account environmental conditions, yet there are external influences to large-scale circulation that we need to consider to refine our analysis. A synoptic-scale event that could be influencing our subsidence regime results is the African Easterly Jet at 700 hPa, which has coastal effects on large-scale circulation (Adebiyi and Zuidema, 2016). Future work could involve observing mean ω_{500} within each $10^{\circ}\times10^{\circ}$ ocean-only domain in the tropical North Atlantic, diagnosing the coastal impacts, and then excluding regions being impacted to refine our analysis.

In order to understand the total radiative impact of convective systems, it would

be useful to determine both the physical and radiative influence of convective systems that formed in zero or relatively weak vertical velocity regimes. Bony et al. (2004) noticed that while individual systems that formed in this domain contributed significantly to Earth's radiation budget, these systems were so prevalent that collectively their influences were significant.

Examining precipitation on its own is useful for diagnosing regional hydrology, but doesn't provide information on how the water cycle is connected to Earth's radiation budget. Studies have looked into combining these features using cloud impact parameters (CIPs) (Daloz et al., 2018). CIPs combine the SW and LW cloud radiative impacts by measuring the strength of the cloud albedo, greenhouse effects, and their ratio. Implementing CIPs would quantify the link between the energetics and hydrological impact of convective systems by measuring how efficiently precipitation radiatively heats the atmosphere and cools the Earth's surface (Daloz et al., 2018).

Igel and van den Heever (2015) noticed the influence that meteorological variables had on convective systems' physical and radiative characteristics. Because convective intensity and precipitation were only weakly sensitive to vertical pressure velocity, it would be interesting to look into other meteorological influences on convective behavior within a single dynamic regime. Sorting behavior by SST and cloud water vapor (CWV) could provide information on the thermodynamics impacting convection. We could also look into how anvil cloud cover responds to increasing SST to determine any aggregate behavior. Using CAPE as another proxy for determining if convection over the ocean is favorable in space and time can provide a more thorough examination of convective

behavior.

In the future, we plan to extend the analysis to the Southern Hemisphere, as well as over land to observe how the behavior and radiative responses of convection change between ocean and land. A comparison of convective behavior over the Atlantic Oean and Pacific Ocean will also be done.

We also seek to track the life cycle of convection to observe how convective processes and their radiative responses change over the life span of a single system (Bouniol et al., 2016, Fiolleau and Roca, 2013, Protopapadaki et al., 2017, Roca et al., 2017). Merging a machine-learning algorithm with the "TOOCAN" technique adapted from Fiolleau and Roca (2013) should quantify how convective regions spread through space and time. Applying our tracking algorithm, we will categorize all such scenes observed over the full 11-year CloudSat mission into developing, mature, and dissipating stages of the convective lifecycle and sort the sensitivity of precipitation and radiative impacts to convective intensity and area accordingly. We will analyze the characteristics of convection in relation to convective life cycle to find the dominant physical processes in each stage. We expect that the precipitation contribution will be largest during the mature stage, while the enhanced positive LW cloud forcing may be largest during the dissipating stage. With this algorithm and the convective attributes described in the first task, we will have a more accurate depiction of how the size and duration of convective cores, precipitating regions, thick anvils, and thin cirrus evolve over the different stages of convective organization. We will also be able to determine how these characteristics and the corresponding precipitation and radiative impacts at different stages of storm maturity vary

with environmental conditions, which will test the implications of convective aggregation.

Both our current and future analyses provide useful metrics for assessing the representation of the relationships between precipitation and radiative impacts and, therefore, the processes that drive them in models. This will be demonstrated by implementing identical diagnostics in the Regional Atmospheric Modeling System (RAMS), which is a large-domain Cloud Resolving Model (CRM) that assumes radiative-convective equilibrium (Cotton et al., 2003). The model will simulate observations of the system with varying environmental conditions and microphysics that we will use to calculate the relationships between precipitation and radiative impacts of convective systems. These relationships will be compared to observations to ensure the initial model state is similar to reality. Finally, we will examine perturbations as a result of CO2 increases.

Bibliography

Adebiyi, A. A. and P. Zuidema, 2016: The role of the southern african easterly jet in modifying the southeast atlantic aerosol and cloud environments. *Quarterly Journal of the Royal Meteorological Society*, **142**, 1574–1589, doi:10.1002/qj.2765.

Allen, M. R. and W. J. Ingram, 2002: Constraints on future changes in climate and the hydrologic cycle. *Nature*, **419**, 228–232, doi:10.1038/nature01092.

Arkin, P. A., 1979: The Relationship between Fractional Coverage of High Cloud and Rainfall Accumulations during GATE over the B-Scale Array. *Monthly Weather Review*, **107**, 1382, doi:10.1175/1520-0493(1979)107¡1382:TRBFCO¿2.0.CO;2.

Arkin, P. A. and B. N. Meisner, 1987: The relationship between large-scale convective rainfall and cold cloud over the western hemisphere during 1982-84. *Monthly Weather Review*, **115**, 51–74, doi:10.1175/1520-0493(1987)115¡0051:TRBLSC¿2.0.CO;2.

Bony, S., G. Bellon, D. Klocke, S. Sherwood, S. Fermepin, and S. Denvil, 2013: Robust direct effect of carbon dioxide on tropical circulation and regional precipitation. *Nature Geoscience*, **6**, 447–451, doi:10.1038/ngeo1799.

Bony, S., R. Colman, V. M. Kattsov, R. P. Allan, C. S. Bretherton, J.-L. Dufresne, A. Hall, S. Hallegatte, M. M. Holland, and W. Ingram, 2006: How Well Do We Understand and Evaluate Climate Change Feedback Processes? *Journal of Climate*, **19**, 3445, doi:10.1175/JCLI3819.1.

Bony, S., J.-L. Dufresne, H. Le Treut, J.-J. Morcrette, and C. Senior, 2004: On dynamic and thermodynamic components of cloud changes. *Climate Dynamics*, **22**, 71–86, doi:10.1007/s00382-003-0369-6.

Bony, S., K.-M. Lau, and Y. C. Sud, 1997: Sea surface temperature and large-scale circulation influences on tropical greenhouse effect and cloud radiative forcing. *Journal of Climate*, **10**, 2055–2077, doi:10.1175/1520-0442(1997)010<2055:SSTALS>2.0.CO;2.

Bony, S., B. Stevens, D. Coppin, T. Becker, K. A. Reed, A. Voigt, and B. Medeiros, 2016: Thermodynamic control of anvil cloud amount. *Proceedings of the National Academy of Science*, **113**, 8927–8932, doi:10.1073/pnas.1601472113.

Bony, S., B. Stevens, D. M. W. Frierson, C. Jakob, M. Kageyama, R. Pincus, T. G. Shepherd, S. C. Sherwood, A. P. Siebesma, A. H. Sobel, M. Watanabe, and M. J. Webb, 2015: Clouds, circulation and climate sensitivity. *Nature Geoscience*, **8**, 261–268, doi:10.1038/ngeo2398.

Bouniol, D., R. Roca, T. Fiolleau, and D. E. Poan, 2016: Macrophysical, microphysical, and radiative properties of tropical mesoscale convective systems over their life cycle. *J. Clim.*, **29**, 3353–3371, doi:10.1175/JCLI-D-15-0551.1.

Bretherton, C. S., P. N. Blossey, and M. Khairoutdinov, 2005: An Energy-Balance Analysis of Deep Convective Self-Aggregation above Uniform SST. *Journal of the Atmospheric Sciences*, **62**, 4273–4292, doi:10.1175/JAS3614.1.

Byrne, M. P., A. G. Pendergrass, A. D. Rapp, and K. R. Wodzicki, 2018: Response of the intertropical convergence zone to climate change: Location, width, and strength. *Current Climate Change Reports*, **4**, 355–370, doi:10.1007/s40641-018-0110-5.

Byrne, M. P. and T. Schneider, 2016a: Energetic Constraints on the Width of the Intertropical Convergence Zone. *Journal of Climate*, **29**, 4709–4721, doi:10.1175/JCLI-D-15-0767.1.

— 2016b: Narrowing of the ITCZ in a warming climate: Physical mechanisms. , **43**, 11,350–11,357, doi:10.1002/2016GL070396.

Chadwick, R., I. Boutle, and G. Martin, 2013: Spatial Patterns of Precipitation Change in CMIP5: Why the Rich Do Not Get Richer in the Tropics. *Journal of Climate*, **26**, 3803–3822, doi:10.1175/JCLI-D-12-00543.1.

Coppin, D. and S. Bony, 2015: Physical mechanisms controlling the initiation of convective self-aggregation in a general circulation model. *Journal of Advances in Modeling Earth Systems*, **7**, 2060–2078, doi:10.1002/2015MS000571.

Cotton, W. R., R. A. Pielke Sr., R. L. Walko, G. E. Liston, C. J. Tremback, H. Jiang, R. L. McAnelly, J. Y. Harrington, M. E. Nicholls, G. G. Carrio, and J. P. McFadden,

2003: RAMS 2001: Current status and future directions. *Meteorology and Atmospheric Physics*, **82**, 5–29, doi:10.1007/s00703-001-0584-9.

Daloz, A. S., E. Nelson, T. L'Ecuyer, A. D. Rapp, and L. Sun, 2018: Assessing the Coupled Influences of Clouds on the Atmospheric Energy and Water Cycles in Reanalyses with A-Train Observations. *Journal of Climate*, **31**, 8241–8264, doi:10.1175/JCLI-D-17-0862.1.

Dessler, A. E., 2013: Observations of Climate Feedbacks over 2000–10 and Comparisons to Climate Models. *Journal of Climate*, **26**, 333–342, doi:10.1175/JCLI-D-11-00640.1.

Emanuel, K. A., 1994: *Atmospheric convection*. Oxford University Press.

Fiolleau, T. and R. Roca, 2013: An Algorithm for the Detection and Tracking of Tropical Mesoscale Convective Systems Using Infrared Images From Geostationary Satellite. *IEEE Trans. Geosci. Remote Sens.*, **51**, 4302–4315, doi:10.1109/TGRS.2012.2227762.

Foster, M. J. and A. Heidinger, 2013: Patmos-x: Results from a diurnally corrected 30-yr satellite cloud climatology. *Journal of Climate*, **26**, 414–425, doi:10.1175/JCLI-D-11-00666.1.

Gettelman, A., M. L. Salby, and F. Sassi, 2002: Distribution and influence of convection in the tropical tropopause region. *Journal of Geophysical Research (Atmospheres)*, **107**, 4080, doi:10.1029/2001JD001048.

Gordon, H. B., P. H. Whetton, A. B. Pittock, A. M. Fowler, and M. R. Haylock, 1992: Simulated changes in daily rainfall intensity due to the enhanced greenhouse effect: implications for extreme rainfall events. *Climate Dynamics*, **8**, 83–102, doi:10.1007/BF00209165.

Hall, T. J. and T. H. Vonder Haar, 1999: The Diurnal Cycle of West Pacific Deep Convection and Its Relation to the Spatial and Temporal Variation of Tropical MCSs. *Journal of Atmospheric Sciences*, **56**, 3401–3415, doi:10.1175/1520-0469(1999)056<3401:TDCOWP>2.0.CO;2.

Hartmann, D. L. and M. L. Michelsen, 1993: Large-Scale Effects on the Regulation of Tropical Sea Surface Temperature. *Journal of Climate*, **6**, 2049–2062, doi:10.1175/1520-0442(1993)006¡2049:LSEOTR¿2.0.CO;2.

Hartmann, D. L. and M. L. Michelsen, 2002: No evidence for iris. *Bulletin of the American Meteorological Society*, **83**, 249–254, doi:10.1175/1520-0477(2002)083<0249:NEFI>2.3.CO;2.

Heidinger, A. K., A. T. Evan, M. J. Foster, and A. Walther, 2012: A naive Bayesian cloud-detection scheme derived from Calipso and applied within PATMOS-x. *J. Appl. Meteorol. Climatol.*, **51**, 1129–1144, doi:10.1175/JAMC-D-11-02.1.

Heidinger, A. K., M. J. Foster, A. Walther, and X. T. Zhao, 2014: The pathfinder atmospheres–extended avhrr climate dataset. *Bulletin of the American Meteorological Society*, **95**, 909–922, doi:10.1175/BAMS-D-12-00246.1.

Heidinger, A. K. and M. J. Pavolonis, 2009: Gazing at cirrus clouds for 25 years through a split window. part i: Methodology. *Journal of Applied Meteorology and Climatology*, **48**, 1100–1116, doi:10.1175/2008JAMC1882.1.

Held, I. M. and B. J. Soden, 2006: Robust Responses of the Hydrological Cycle to Global Warming. *Journal of Climate*, **19**, 5686, doi:10.1175/JCLI3990.1.

Henderson, D. S., T. L'Ecuyer, G. Stephens, P. Partain, and M. Sekiguchi, 2013: A multisensor perspective on the radiative impacts of clouds and aerosols. *Journal of Applied Meteorology and Climatology*, **52**, 853–871, doi:10.1175/JAMC-D-12-025.1.

Houze, R. A., 2004: Mesoscale convective systems. *Reviews of Geophysics*, **42**, RG4003, doi:10.1029/2004RG000150.

Houze Jr., R. A., 1982: Cloud clusters and large-scale vertical motions in the tropics. *Journal of the Meteorological Society of Japan. Ser. II*, **60**, 396–410, doi:10.2151/jmsj1965.60.1$_3$96.

Igel, M. R., A. J. Drager, and S. C. van den Heever, 2014: CloudSat cloud object partitioning technique and assessment and integration of deep conevctive anvil sensitivities to SST. *Journal of Geophysical Research : Atmospheres*, **119**, 515–535, doi:10.1002/2014JD021717.Received.

Igel, M. R. and S. C. van den Heever, 2015: The relative influence of environmental characteristics on tropical deep convective morphology as observed by CloudSat. *J. Geophys. Res.*, **120**, 4304–4322.

IPCC, 2013: *Summary for Policymakers*, Cambridge University Press, Cambridge, United Kingdom and New York, NY, USA, book section SPM. 1–30.

Knutson, T. R. and S. Manabe, 1995: Time-Mean Response over the Tropical Pacific to Increased $C0_2$ in a Coupled Ocean-Atmosphere Model. *Journal of Climate*, **8**, 2181–2199, doi:10.1175/1520-0442(1995)008¡2181:TMROTT¿2.0.CO;2.

Kubar, T. L., D. L. Hartmann, and R. Wood, 2007: Radiative and Convective Driving of Tropical High Clouds. *Journal of Climate*, **20**, 5510–5526, doi:10.1175/2007JCLI1628.1.

Lau, K. M. and H. T. Wu, 2007: Detecting trends in tropical rainfall characteristics, 1979 2003. *International Journal of Climatology*, **27**, 979–988, doi:10.1002/joc.1454.

Lau, W. K. M. and K.-M. Kim, 2015: Robust Hadley Circulation changes and increasing global dryness due to CO_2 warming from CMIP5 model projections. *Proceedings of the National Academy of Science*, **112**, 3630–3635, doi:10.1073/pnas.1418682112.

L'Ecuyer, T. S., W. Berg, J. Haynes, M. Lebsock, and T. Takemura, 2009: Global observations of aerosol impacts on precipitation occurrence in warm maritime clouds. *Journal of Geophysical Research: Atmospheres*, **114**, doi:10.1029/2008JD011273.

L'Ecuyer, T. S., N. B. Wood, T. Haladay, G. L. Stephens, and P. W. Stackhouse Jr., 2008: Impact of clouds on atmospheric heating based on the r04 cloudsat fluxes and heating rates data set. *Journal of Geophysical Research: Atmospheres*, **113**, doi:10.1029/2008JD009951.

Li, Y., D. W. J. Thompson, G. L. Stephens, and S. Bony, 2014: A global survey of the instantaneous linkages between cloud vertical structure and large-scale climate. *Journal of Geophysical Research (Atmospheres)*, **119**, 3770–3792, doi:10.1002/2013JD020669.

Lindzen, R. S., M. D. Chou, and A. Y. Hou, 2001: Does the Earth Have an Adaptive Infrared Iris? *Bull. Am. Meteorol. Soc.*, **82**, 417–432, doi:10.1175/1520-0477(2001)082<0417:DTEHAA>2.3.CO;2.

Liou, K.-N., 1986: Influence of Cirrus Clouds on Weather and Climate Processes: A Global Perspective. *Monthly Weather Review*, **114**, 1167, doi:10.1175/1520-0493(1986)114<1167:IOCCOW>2.0.CO;2.

Liu, C. and E. Zipser, 2013: Regional variation of morphology of organized convection in the tropics and subtropics. *Journal of Geophysical Research (Atmospheres)*, **118**, 453–466, doi:10.1029/2012JD018409.

Liu, C. and E. J. Zipser, 2005: Global distribution of convection penetrating the tropical tropopause. *Journal of Geophysical Research (Atmospheres)*, **110**, D23104, doi:10.1029/2005JD006063.

Liu, C., E. J. Zipser, and S. W. Nesbitt, 2007: Global Distribution of Tropical Deep Convection: Different Perspectives from TRMM Infrared and Radar Data. *Journal of Climate*, **20**, 489, doi:10.1175/JCLI4023.1.

Lu, J., G. A. Vecchi, and T. Reichler, 2007: Expansion of the Hadley cell under global warming. , **34**, L06805, doi:10.1029/2006GL028443.

Mapes, B. E. and R. A. Houze, 1993: Cloud Clusters and Superclusters over the Oceanic Warm Pool. *Monthly Weather Review*, **121**, 1398, doi:10.1175/1520-0493(1993)121<1398:CCASOT>2.0.CO;2.

Mauritsen, T. and B. Stevens, 2015: Missing iris effect as a possible cause of muted hydrological change and high climate sensitivity in models. *Nature Geoscience*, **8**, 346–351, doi:10.1038/ngeo2414.

Merlis, T. M., 2015: Direct weakening of tropical circulations from masked CO_2 radiative forcing. *Proceedings of the National Academy of Science*, **112**, 13167–13171, doi:10.1073/pnas.1508268112.

Mitchell, J. F. B., 1987: Detection of climate change due to increases in CO_2 and trace gases. *Theoretical and Applied Climatology*, **38**, 234–234, doi:10.1007/BF00867416.

Mohr, K. I. and E. J. Zipser, 1996: Defining Mesoscale Convective Systems by Their 85-GHz Ice-Scattering Signatures. *Bulletin of the American Meteorological Society*, **77**, 1179–1190, doi:10.1175/1520-0477(1996)077<1179:DMCSBT>2.0.CO;2.

Muller, C. J. and I. M. Held, 2012: Detailed investigation of the self-aggregation of convection in cloud-resolving simulations. *Journal of the Atmospheric Sciences*, **69**, 2551–2565, doi:10.1175/JAS-D-11-0257.1.

Nesbitt, S. W., R. Cifelli, and S. A. Rutledge, 2006: Storm Morphology and Rainfall Characteristics of TRMM Precipitation Features. *Monthly Weather Review*, **134**, 2702, doi:10.1175/MWR3200.1.

Nesbitt, S. W., E. J. Zipser, and D. J. Cecil, 2000: A Census of Precipitation Features in the Tropics Using TRMM: Radar, Ice Scattering, and Lightning Observations. *Journal of Climate*, **13**, 4087–4106, doi:10.1175/1520-0442(2000)013<4087:ACOPFI>2.0.CO;2.

Nilsson, J. and K. A. Emanuel, 1999: Equilibrium atmospheres of a two-column radiative-convective model. *Q. J. R. Meteorol. Soc.*, **125**, 2239–2264.

Pierrehumbert, R. T., 1995: Thermostats, Radiator Fins, and the Local Runaway Greenhouse. *Journal of Atmospheric Sciences*, **52**, 1784–1806, doi:10.1175/1520-0469(1995)052¡1784:TRFATL¿2.0.CO;2.

Protopapadaki, S. E., C. J. Stubenrauch, and A. G. Feofilov, 2017: Upper tropospheric cloud systems derived from IR sounders: Properties of cirrus anvils in the tropics. *Atmos. Chem. Phys.*, **17**, 3845–3859, doi:10.5194/acp-17-3845-2017.

Ramanathan, V. and W. Collins, 1991: Thermodynamic regulation of ocean warming by cirrus clouds deduced from observations of the 1987 El Niño. *Nature*, **351**, 27–32.

Randall, D. A., Harshvardhan, D. A. Dazlich, and T. G. Corsetti, 1989: Interactions among Radiation, Convection, and Large-Scale Dynamics in a General Circulation Model. *Journal of Atmospheric Sciences*, **46**, 1943–1970, doi:10.1175/1520-0469(1989)046<1943:IARCAL>2.0.CO;2.

Riehl, H. and J. S. Malkus, 1958: On the heat balance in the equatorial trough zone. *Geophysica*, **6**, 503–538.

Riehl, H. and J. Simpson, 1979: The heat balance of the equatorial trough zone, revisited. *Beitraege zur Physik der Atmosphaere*, **52**, 287–305.

Rienecker, M. M., M. Suarez, R. Todling, J. Bacmeister, L. Takacs, H. Liu, W. Gu, M. Sienkiewicz, R. Koster, R. Gelaro, et al., 2008: The geos-5 data assimilation system: Documentation of versions 5.0. 1, 5.1. 0, and 5.2. 0.

Rienecker, M. M., M. J. Suarez, R. Gelaro, R. Todling, J. Bacmeister, E. Liu, M. G. Bosilovich, S. D. Schubert, L. Takacs, G.-K. Kim, S. Bloom, J. Chen, D. Collins, A. Conaty, A. da Silva, W. Gu, J. Joiner, R. D. Koster, R. Lucchesi, A. Molod, T. Owens, S. Pawson, P. Pegion, C. R. Redder, R. Reichle, F. R. Robertson, A. G. Ruddick, M. Sienkiewicz, and J. Woollen, 2011: Merra: Nasa's modern-era retrospective analysis for research and applications. *Journal of Climate*, **24**, 3624–3648, doi:10.1175/JCLI-D-11-00015.1.

Roca, R., T. Fiolleau, and D. Bouniol, 2017: A Simple Model of the Life Cycle of Mesoscale Convective Systems Cloud Shield in the Tropics. *J. Clim.*, **30**, 4283–4298, doi:10.1175/JCLI-D-16-0556.1.

URL `http://journals.ametsoc.org/doi/10.1175/JCLI-D-16-0556.1`

Rossow, W. B. and R. A. Schiffer, 1999: Advances in Understanding Clouds from ISCCP. *Bulletin of the American Meteorological Society*, **80**, 2261–2288, doi:10.1175/1520-0477(1999)080<2261:AIUCFI>2.0.CO;2.

Schmetz, J., P. Pili, S. Tjemkes, D. Just, J. Kerkmann, S. Rota, and A. Ratier, 2002: An introduction to meteosat second generation (msg). *Bulletin of the American Meteorological Society*, **83**, 977–992, doi:10.1175/1520-0477(2002)083¡0977:AITMSG¿2.3.CO;2.

Schumacher, C. and J. Houze, Robert A., 2003: Stratiform Rain in the Tropics as Seen by the TRMM Precipitation Radar(. *Journal of Climate*, **16**, 1739–1756, doi:10.1175/1520-0442(2003)016<1739:SRITTA>2.0.CO;2.

Sherwood, S. C., S. Bony, and J.-L. Dufresne, 2014: Spread in model climate sensitivity traced to atmospheric convective mixing. *Nature*, **505**, 37.

Slingo, A. and J. M. Slingo, 1988: The response of a general circulation model to cloud longwave radiative forcing. I: Introduction and initial experiments. *Quarterly Journal of the Royal Meteorological Society*, **114**, 1027–1062, doi:10.1002/qj.49711448209.

— 1991: Response of the National Center for Atmospheric Research community climate model to improvements in the representation of clouds. *Journal of Geophysical Research*, **96**, 15,341–15,357, doi:10.1029/91JD00930.

Smalley, M., T. L'Ecuyer, M. Lebsock, and J. Haynes, 2014: A comparison of precipitation occurrence from the ncep stage iv qpe product and the cloudsat cloud profiling radar. *Journal of Hydrometeorology*, **15**, 444–458, doi:10.1175/JHM-D-13-048.1.

Stephens, G. L. and T. D. Ellis, 2008: Controls of global-mean precipitation increases in global warming GCM experiments. *J. Clim.*, **21**, 6141–6155, doi:10.1175/2008JCLI2144.1.

Stevens, B. and S. Bony, 2013: What Are Climate Models Missing? *Science*, **340**, 1053–1054, doi:10.1126/science.1237554.

Storer, R. L., S. C. Van Den Heever, and T. S. L'Ecuyer, 2014: Observations of aerosol-induced convective invigoration in the tropical east Atlantic. *J. Geophys. Res.*, **119**, 3963–3975, doi:10.1002/2013JD020272.

Sun, B., M. Free, H. L. Yoo, M. J. Foster, A. Heidinger, and K. G. Karlsson, 2015: Variability and trends in U.S. cloud cover: ISCCP, PATMOS-x, and CLARA-A1 compared to homogeneity-adjusted weather observations. *J. Clim.*, **28**, 4373–4389, doi:10.1175/JCLI-D-14-00805.1.

Tan, J., C. Jakob, W. B. Rossow, and G. Tselioudis, 2015: Increases in tropical rainfall driven by changes in frequency of organized deep convection. *Nature*, **519**, 451–454, doi:10.1038/nature14339.

Tobin, I., S. Bony, C. E. Holloway, and J.-y. Grandpeix, 2013: Does convective aggregation need to be represented in cumulus parameterizations? *Journal of Advances in Modeling Earth Systems*, **5**, 692–703, doi:10.1002/jame.20047.

Tobin, I., S. Bony, and R. Roca, 2012: Observational evidence for relationships between the degree of aggregation of deep convection, water vapor, surface fluxes, and radiation. *Journal of Climate*, **25**, 6885–6904, doi:10.1175/JCLI-D-11-00258.1.

Tselioudis, G., E. Tromeur, W. B. Rossow, and C. S. Zerefos, 2010: Decadal changes in tropical convection suggest effects on stratospheric water vapor. *Geophysical Research Letters*, **37**, L14806, doi:10.1029/2010GL044092.

Wallace, J. M. and P. V. Hobbs, 2006: *Atmospheric science: an introductory survey*. Elsevier Academic Press, 2 edition.

Walther, A. and A. K. Heidinger, 2012: Implementation of the daytime cloud optical and microphysical properties algorithm (dcomp) in patmos-x. *Journal of Applied Meteorology and Climatology*, **51**, 1371–1390, doi:10.1175/JAMC-D-11-0108.1.

Walther, A., A. K. Heidinger, and S. Miller, 2013: The expected performance of cloud optical and microphysical properties derived from suomi npp viirs day/night band lunar reflectance. *Journal of Geophysical Research: Atmospheres*, **118**, 13,230–13,240, doi:10.1002/2013JD020478.

Wing, A. A. and T. W. Cronin, 2016: Self-aggregation of convection in long channel geometry. *Quarterly Journal of the Royal Meteorological Society*, **142**, 1–15, doi:10.1002/qj.2628.

Wing, A. A. and K. A. Emanuel, 2014: Journal of advances in modeling earth systems convection in idealized numerical modeling simulations. *Journal of Advances in Modeling Earth Systems*, **6**, 59–74, doi:10.1002/2013MS000269.

Zelinka, M. D. and D. L. Hartmann, 2009: Response of humidity and clouds to tropical deep convection. *Journal of Climate*, **22**, 2389–2404, doi:10.1175/2008JCLI2452.1.